CANCER

Modulation of blood-tumor barrier transcriptional programs improves intratumoral drug delivery and potentiates chemotherapy in GBM

Jorge L. Jimenez-Macias[1,2], Philippa Vaughn-Beaucaire[1,2], Ayush Bharati[1], Zheyun Xu[1], Megan Forrest[1], Jason Hong[1], Michael Sun[1], Andrea Schmidt[1], Jasmine Clark[1], William Hawkins[1], Noe Mercado[1], Jacqueline Real[1], Kelsey Huntington[1], Mykola Zdioruk[3], Michal O. Nowicki[3], Choi-Fong Cho[3,4,5], Bin Wu[6], Weiyi Li[7], Theresa Logan[7], Katherine E. Manz[8], Kurt D. Pennell[8], Bogdan I. Fedeles[9], Paul Bertone[1,10], Michael Punsoni[11], Alexander S. Brodsky[1]†, Sean E. Lawler[1]*

Efficient drug delivery to glioblastoma (GBM) is a major obstacle as the blood-brain barrier (BBB) and the blood-tumor barrier (BTB) prevent passage of the majority of chemotherapies into the brain. Here, we identified a transcriptional 12-gene signature associated with the BTB in GBM. We identified CDH5 as a core molecule in this set and confirmed its expression in GBM vasculature using transcriptomics and immunostaining of patient specimens. The indirubin-derivative, 6-bromoindirubin acetoxime (BIA), down-regulates CDH5 and other BTB signature genes, causing endothelial barrier disruption in vitro and in murine GBM xenograft models. Treatment with BIA increased intratumoral cisplatin accumulation and potentiated DNA damage by targeting DNA repair pathways. Last, using an injectable BIA nanoparticle formulation, PPRX-1701, we significantly improved cisplatin efficacy in murine GBM. Our work reveals potential targets of the BTB and the bifunctional properties of BIA as a BTB modulator and a potentiator of chemotherapy, supporting its further development.

INTRODUCTION

The effective treatment of brain malignancies such as glioblastoma (GBM), remains a critical challenge in the neuro-oncology field. GBM is the most common malignant primary brain tumor, representing ~15% of all central nervous system (CNS) neoplasms (*1*). Median survival is 15 to 18 months, and less than 10% of patients survive beyond 5 years after diagnosis (*2*). The standard of care involves maximal safe surgical resection, followed by radiotherapy and alkylating chemotherapy with temozolomide (TMZ). This inevitably leads to the development of untreatable recurrent disease. The major challenges in GBM therapy are (i) its invasiveness, which prevents complete surgical resection, (ii) high levels of intratumoral molecular and cellular heterogeneity, (iii) a cancer-promoting tumor microenvironment, and (iv) the presence of the blood-brain barrier (BBB) and blood-brain tumor barrier (BTB), which limit drug entry.

The BBB maintains homeostasis of the CNS for its proper functioning (*3*). In an oncogenic context, the BBB responds to cues by the cancer cells, which promote the formation of new blood vessels and the BTB. The BTB is a distinct and heterogeneous biological entity, resulting from cellular interactions between brain tumor cells, newly formed blood vessels, and the preexisting BBB (*4*). Molecular characteristics that define the impermeability of the BBB, such as tight junction and adherens junction formation, high efflux pump expression, and nonfenestrated endothelium, are compromised in brain tumors mainly due to hypoxic/angiogenic conditions, which also promote tumor growth, migration, and invasion (*5*). Regardless of the disruption of these brain-protecting BBB properties, non-BBB penetrant drugs still do not penetrate GBM tissue efficiently. This is supported by studies suggesting that the BTB is highly heterogeneous (*6*), with some regions maintaining "healthy" BBB features that protect GBM cells from antineoplastic agent accumulation.

The BTB remains poorly understood, especially its molecular and cellular composition and identification of target molecular pathways that could render it permissive to chemotherapy uptake. Strategies to improve drug delivery to GBM include focused ultrasound (*7*, *8*), convection-enhanced delivery (*9*), optogenetics (*10*), systemic administration of drug-loaded nanoparticles (*11*), and drug-conjugated cell-penetrating peptides (*12*), with most of these showing promising preclinical results. These strategies rely on physically overcoming the BBB/BTB and have advantages of controlled release, preservation of drug stability, and drug delivery at selected anatomical sites. In addition to these approaches, the identification of compounds that could target molecular elements that selectively regulate BTB permeability, but not healthy BBB, would enable mechanistic control over the biological processes involving the BTB/GBM tumor interactions and could be used to potentiate intratumoral drug penetration. Moreover, if these compounds could simultaneously hinder tumor development and synergize with chemotherapeutic regimens, then this would be potentially useful in the clinic.

Previously, we identified the anti-invasive and immunomodulatory properties of the indirubin-derivative 6-bromoindirubin acetoxime

[1]Legorreta Cancer Center, Department of Pathology and Laboratory Medicine, Brown University, Providence, RI 02903, USA. [2]Department of Chemistry, Massachusetts Institute of Technology, Cambridge, MA 02139, USA. [3]Harvey Cushing Neuro-Oncology Laboratories, Department of Neurosurgery, Brigham and Women's Hospital, Harvard Medical School, Boston, MA 02115, USA. [4]Program in Neuroscience, Harvard Medical School, Boston, MA 02115, USA. [5]Harvard Stem Cell Institute, Harvard University, Boston, MA 02115, USA. [6]Cytodigm Inc, Natick, MA 01760, USA. [7]Phosphorex Inc, Hopkinton, MA 01748, USA. [8]School of Engineering, Brown University, Providence, RI 02912, USA. [9]Center for Environmental Health Sciences, Massachusetts Institute of Technology, Cambridge, MA 02139, USA. [10]Department of Medicine, Brown University, Providence, RI 02903, USA. [11]Brown University Health, Warren Alpert Medical School, Providence, RI 02903, USA.
*Corresponding author. Email: sean_lawler@brown.edu
†Deceased.

(BIA) in GBM and showed some benefit in murine GBM models (*13*). We also developed a BIA-loaded nanoparticle formulation, PPRX-1701, which was well-tolerated, and able to reach intracranial brain tumors in mouse models. Indirubins are bisindole alkaloid compounds used as a component of traditional Chinese medicine for the treatment of proliferative disorders and autoimmune conditions. Indirubin is a component from the *Indigo naturalis* extract (*14*). BIA is widely known as a GSK-3 inhibitor (*15*), but several other kinases have been found to be inhibited by this compound, including cyclin-dependent kinases and Src family kinases (*16*).

Here, we report that BIA has significant effects on BTB permeability by reducing the expression of BTB signature genes, including the tight junction protein CDH5 [vascular endothelial cadherin (VE-cadherin)]. BIA treatment increased cisplatin accumulation in tumor tissue in mouse tumor models, but not in healthy brain, and enhanced the cytotoxic capacity of cisplatin. BIA in combination with cisplatin prolonged survival of xenograft GBM models. Together, our work provides evidence of potential candidate targets at the BTB and the use of BIA for improved drug delivery and chemotherapy potentiation in GBM.

RESULTS

Identification of GBM endothelium–enriched transcripts via in silico screening

The BTB represents an obstacle to therapeutic drug delivery and remains a poorly defined component of GBM biology. Thus, to identify molecular signatures of the GBM vasculature for targeting of the BTB, we performed an in silico–based approach by accessing bulk RNA sequencing (RNA-seq) data from The Cancer Genome Atlas, Rembrandt, and the Ivy Glioblastoma Atlas Project (IVY GAP) databases (Fig. 1A). In the cBio portal, we used Spearman's rank correlation to select GBM genes that showed coexpression with four well-characterized endothelial cell reference transcripts defined by Dusart *et al.* (*17*) for screening brain tumor–associated vascular gene expression signatures: Platelet Endothelial Cell Adhesion Molecule-1 (*PECAM1*)/*CD31*, *CD34*, Von Willebrand Factor (*VWF*), and C-lectin 14A (*CLEC14A)* (table S1). Next, we used the Rembrandt dataset for identifying those genes of this list enriched in GBM tissue above healthy controls and lastly identified their tumoral regional expression by using the IVY GAP resource, a laser microdissection-based RNA-seq bulk dataset obtained from clinical specimens. With this approach, we identified a signature composing of 12 GBM endothelium–enriched genes (Fig. 1B). These genes present abundant expression at microvascular proliferation regions in the tumor (Fig. 1C). Gene Ontology (GO) analysis revealed their primary involvement in vasculature system development, morphogenesis, cell migration, and responses to transforming growth factor–β (TGF-β) pathway activation and positive regulation of receptor serine/threonine kinase signaling (Fig. 1D). Search Tool for the Retrieval of Interacting Genes (STRING) network analysis showed that the genes form significant interactions within the network [protein-protein interaction (PPI) enrichment *P* value: $<1.0 \times 10^{-16}$]. With the exception of *MYO1B*, all genes were interconnected (Fig. 1E), suggesting strong functional relationships within the identified signature gene set. To confirm endothelial-associated specificity of the identified 12-gene network, we reperformed our analysis using *PECAM1* and *VWF* only as probe marker genes. This led to a reduced list of six genes that were also identified using the Dusart *et al.* markers (*17*): *ACVRL1*, *CD93*, *ENG*, *ENPEP*, *MYO1B*, and *PCDH12* (fig. S1, A to C). Analysis of *CD34* and *CLEC14A* expression using the IVY GAP resource showed enrichment of these genes at microvascular proliferative regions (fig. S1D), supporting their regional enrichment at the GBM-associated vasculature.

Given the pleiotropic nature of these identified transcripts, as well as some known nonvascular functions, the possibility that our bulk RNA-seq–based analysis is providing transcript signals from other cell types is feasible. To address this, we consulted a recently published single-cell brain vasculature atlas by Wälchli *et al.* (*18*). Using a reported interactive website (https://waelchli-lab-human-brain-vasculature-atlas.ethz.ch/), we visualized our used vascular reference markers (*PECAM1*, *VWF*, *CD34*, and *CLEC14A*) and the 12 newly identified GBM endothelium–enriched transcripts from GBM clinical sample–sorted single cells (fig. S2A). Our GBM endothelium–enriched transcripts were highly expressed in endothelial cells above other cell types in the tumor microenvironment, with the exception of *CD93*, *PDGFRB*, and *ENPEP*. *CD93* was seen highly expressed in neutrophils, and *PDGFRB* and *ENPEP*, which expression was mostly seen in pericytes and smooth muscle cells, both which are components of the BBB. Furthermore, there was increased expression of our GBM-enriched signature genes in fluorescence-activated cell sorting (FACS)–sorted GBM endothelia above endothelia of healthy temporal lobe and other brain malignancies such as low-grade glioma, metastases, and meningioma (fig. S2B). We then examined the expression of our endothelial-associated transcripts across different endothelium subtypes from FACS-sorted GBM endothelial cells (fig. S2C). Our findings indicate that angiogenic capillaries have enriched expression of these genes. *MYO1B*, *ENPEP*, and *PDGFRB* were strongly expressed in cells undergoing endothelial-to-mesenchymal transition (EndoMT) and proliferative EndoMT cells, suggesting that these genes are confined to a subset undergoing mesenchymal state transitions.

CDH5 is highly expressed in GBM tumor–associated endothelium

The STRING analysis showed that *CDH5* (VE-cadherin, CD144) may represent a central node in the BTB signature gene network. CDH5 is a calcium-dependent adherens junction protein with a fundamental role in maintaining BBB integrity (*19*). To further investigate its potential role in the BTB of GBM, we reanalyzed spatial transcriptomic data from malignant glioma tissue samples published by Ravi *et al.* (*20*) and confirmed the enriched expression of *CDH5* in comparison to matched nontumor brain cortex tissue UKF_248 (Fig. 2A), UKF_242, UKF_259, and UKF_334 (fig. S3, A to C). *CDH5* was highly expressed in clusters enriched in vascular markers such as *PECAM1* and *VWF* (Fig. 2, A to C, and fig. S3, D to F). However, *CDH5* also enriched in other *PECAM1*-negative clusters, which indicates that CDH5 spatial expression is heterogeneous and occurs in multiple cell types in addition to endothelial cells. *CDH5*-expressing clusters were enriched in Biological Process GOs related to (Fig. 2D) "Regulation of Vasculature Development" and "Angiogenesis" and "Vascular Process in Circulatory System" (fig. S4), supporting its involvement in vascular biology in GBM. Moreover, we identified a list of 61 additional genes regionally coexpressed with *CDH5* (table S2), which includes genes such as *CCL2* (*4*) and *WNT7B* (*21*, *22*), which have reported roles in the BTB and BBB, respectively. To confirm the presence of CDH5 in GBM tumors, we performed immunofluorescence (IF) staining in GBM patient specimens for anti-CDH5 in

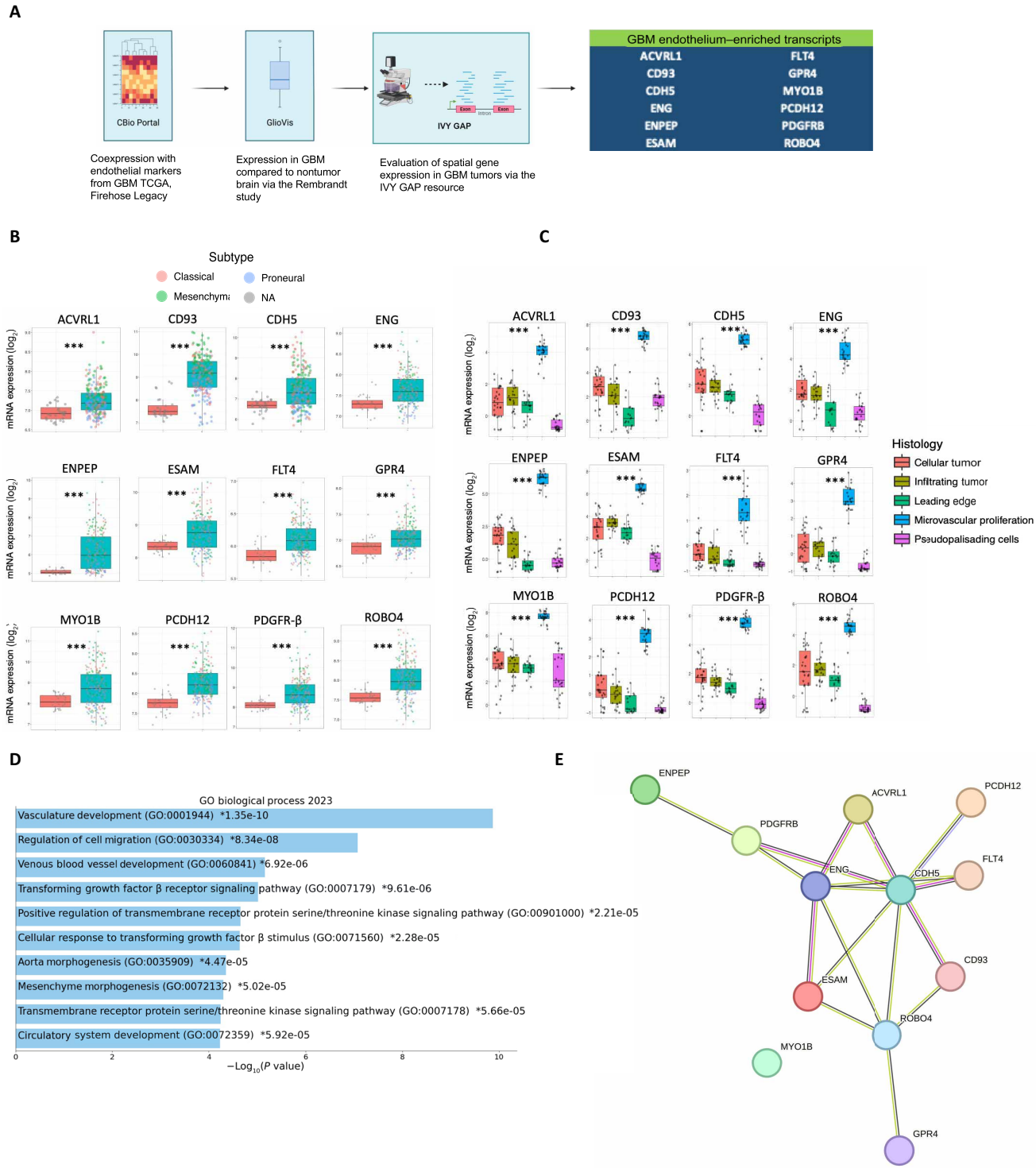

Fig. 1. Identification of tumor-endothelium associated (BTB genes) using bulk RNA-seq datasets from GBM clinical samples. (**A**) Workflow of identification and filtering of genes associated with tumoral vasculature in GBM. Using a gene expression correlation tool, cBio, top 50 genes that coexpressed with CD31, VWF, CD34, and CLEC14A were selected, confirmed their overexpression in tumor above normal brain in the Rembrandt dataset using GlioVis visualization tool, and evaluated regional expression using the IVY GAP atlas resource. Panel figure was generated using Biorender.com. (**B**) Gene expression of 12 GBM endothelium–enriched transcripts identified in the cBio Portal following the workflow shown in (A) ***$P < 0.001$ by Tukey's post hoc test. Individual values are colored by GBM subtypes classical, mesenchymal, or proneural. NA indicates unknown sample information. (**C**) Regional expression of the 12 BTB genes in GBM using the IVY GAP resource. ***$P < 0.001$ by Tukey's post hoc test. (**D**) Gene ontology analysis (GO Biological Process 2023) of the 12 BTB genes using the EnrichR software. Biological processes are ranked by *P* values, which are indicated next to the GO designation. (**E**) STRING network analysis on the 13 identified BTB genes; 12 nodes, 17 edges, average node degree of 2.83. PPI enrichment *P* value, 1×10^{-16}.

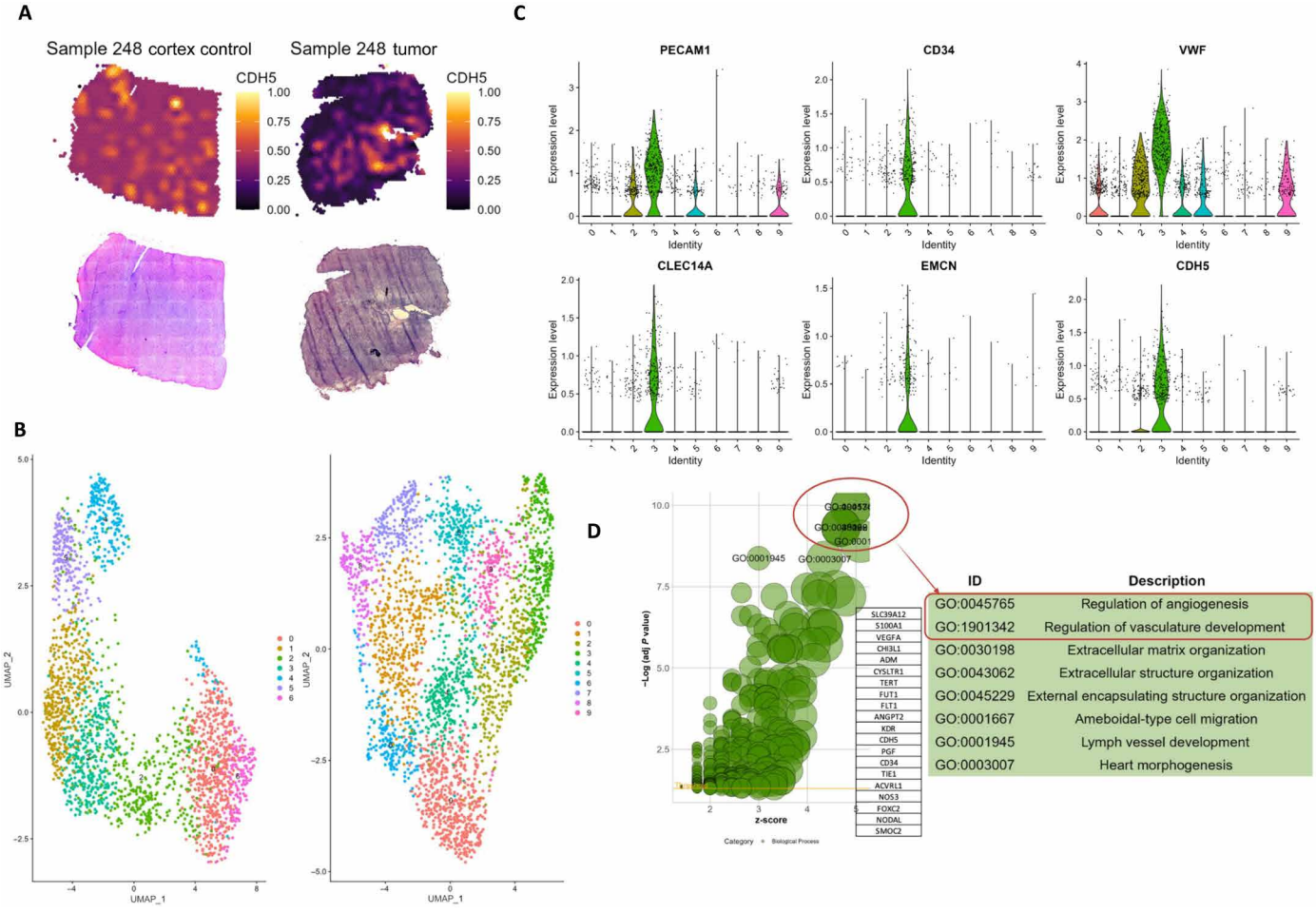

Fig. 2. Spatial transcriptomic analysis of GBM patient samples confirms *CDH5* up-regulation in tumor-associated endothelium. (**A**) Surface plots of CDH5 expression from spatial transcriptomic performed on UKF_248 GBM tumor and nontumorigenic cortex tissues. (**B**) Spatial Uniform Manifold Approximation and Projection (UMAP) clustering plot in cortex (left) and tumor (right) for UKF_248. (**C**) Violin plots indicating endothelial cell marker expression and CDH5 from UKF_248 tissues and clustered according to spatial clustering from (B). (**D**) GO indicating associated pathways with CDH5 gene expression in cluster 3 of sample UKF_248. GO biological processes highlighted in red indicate vasculature development and regulation of angiogenesis as pathways enriched for *CDH5*. Top 20 gene list for highlighted GO pathways is shown. Data were obtained and reanalyzed from (*20*) using the SPATA2 package from R-studio.

combination with anti-CD31. GBM tumors were confirmed in these samples by histology (fig. S5, A to F). We observed CDH5 expression across the tumor specimens (fig. S6, A to F) and present in $CD31^+$ blood vessels as expected, with diverse correlation of coexpression of CD31 and CDH5 across samples (fig. S6G). CD31-negative cells also expressed CDH5. Potentially, tumor cells undergoing vascular mimicry are known to express CDH5 (*23*–*25*). To reveal CDH5 expression heterogeneity in the BTB, we performed IF visualization of CDH5 in $CD31^+$ blood vessels in a patient-derived xenograft GBM model focusing on the tumor core and leading edge regions (fig. S7A). This imaging showed strong expression of CDH5 in not only $CD31^+$ vasculature but also in green fluorescent protein (GFP)–labeled engrafted tumor cells. Pearson correlation analysis did not show any regional difference of CDH5/$CD31^+$ vessel coexpression (fig. S7B). However, CDH5 is significantly more expressed in $CD31^+$ blood vessels than in GFP^+ tumor cells at the core and at the leading edge (fig. S7C), confirming that CDH5 is enriched in tumor-associated vasculature. Together, these data demonstrate the presence of CDH5 in GBM endothelium, where it may play a role in BTB function.

BIA targets BTB-related transcriptional programs in brain endothelial cells

Previously, we demonstrated that BIA has anti-angiogenic effects in murine intracranial models of GBM (*13*). This led us to investigate the transcriptional alterations associated with BIA treatment of brain endothelium. Bulk RNA-seq analysis of a well-characterized human brain microvascular endothelial cell (HBMEC) line, HCMEC/D3, treated with BIA showed considerable transcriptional dysregulation. The top 15 differentially expressed genes (DEGs) are displayed according to significance in a heatmap (Fig. 3A). CDH5 was one of the most down-regulated genes upon BIA treatment (−3.06-fold, $\log_2$). GO analysis of significantly up-regulated (862 genes) and down-regulated (652 genes) differentially expressed transcripts revealed that BIA mostly induced expression of genes in processes related to amino acid transport. BIA also decreased expression of genes involved in annotated processes of cell migration, motility, angiogenesis, and endothelial proliferation, as well as nitric oxide synthesis and pathways of receptor tyrosine kinases (Fig. 3B). Volcano plot analysis (Fig. 3C) of $\log_2$ fold change ($\log_2$FC) versus

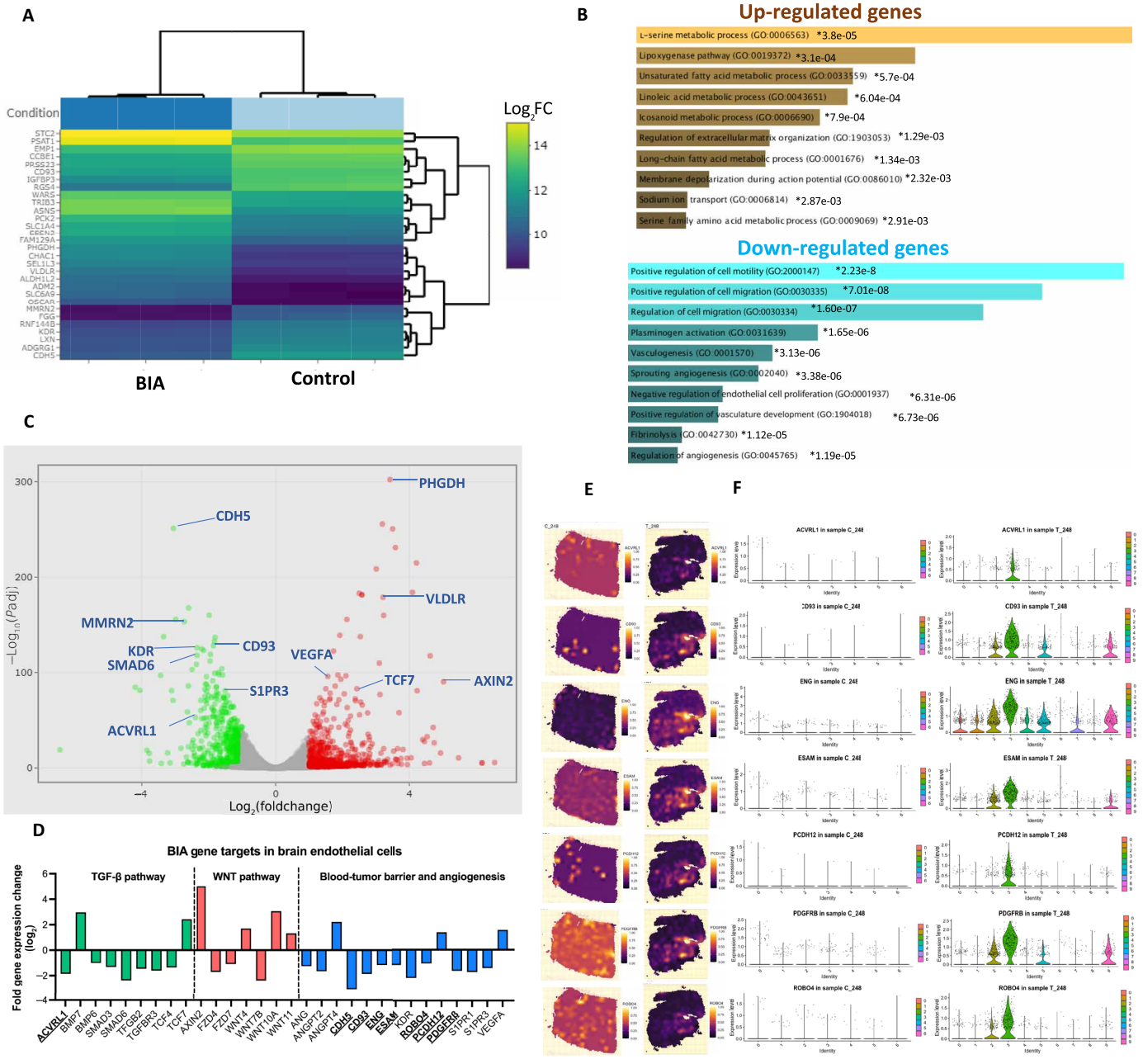

Fig. 3. BIA modulates BTB-associated genes and cell motility, vascular development, angiogenesis, and L-serine metabolism in brain endothelial cells. (**A**) Heatmap generated from the top 15 up-regulated and down-regulated genes (log_2FC) from bulk RNA-seq analysis performed on HCMEC/D3 cells treated with BIA (1 μM, 24 hours). (**B**) GO analysis of >1.5 (log_2FC) significantly up-regulated and down-regulated genes by BIA in brain endothelial cells from (A). Biological processes are ranked by *P* values, which are shown next to the GO designation. Analysis performed using the EnrichR software. (**C**) Volcano plot analysis from all the up-regulated and down-regulated genes by BIA. Labels on genes related to angiogenesis, TGF-β, and WNT pathways are highlighted. (**D**) Gene expression fold change (log_2) levels of dysregulated genes by BIA related to the TGF-β and WNT pathways, angiogenesis, and the tumor vascular associated genes (BTB genes, highlighted). (**E**) Spatial expression of 7 of the 12 BTB genes regulated by BIA in vitro highlighted in (D) for nontumor (left) and tumor (right) tissues from sample UKF_248. (**F**) Clustered gene expression of UKF_248 showing the BTB genes from (E) in nontumor (left) and tumor tissue (right).

P value significance of down-regulated DEGs highlights *CDH5* and other angiogenesis-related genes such as *MMRN2*, a direct interactor with CDH5, CD93, ACVRL1, KDR, SMAD6, and S1PR3. BIA also promoted expression of genes such as *PHGDH*, *AXIN2*, *TCF7*, *VLDLR*, and *VEGFA*, showing that BIA has broad effects on genes involved in diverse pathways. We then examined dysregulated genes that are potentially involved in BTB biology by focusing on BBB permeability/integrity and in biological functions of angiogenesis (Fig. 3D). BIA modulates 8 of our 12 BTB signature genes we identified in the in silico screening from clinical samples (Fig. 3D, highlighted). Most of these genes were down-regulated by BIA, except *PCDH12*, which increased its expression. This finding suggests

that BIA targets the expression of BTB-associated transcriptional programs in brain endothelial cells. Our spatial transcriptomic analysis of sample UKF_248 showed the increased expression of these 12 GBM endothelium–enriched transcripts in GBM clinical samples above cortex controls (Fig. 3E) and spatially coexpressed to endothelial markers by clustering analysis (Fig. 3F). These genes were expressed across different tumor samples (fig. S8) and indicate the relevance of these pathways in GBM.

BIA disrupts barrier formation in BBB models in vitro

Given the prominence of CDH5 in the BTB transcriptome and its known role of maintaining vascular barrier integrity, we focused our efforts in further characterizing CDH5 expression in the endothelium upon BIA treatment. IF staining of CDH5 showed a marked decrease at the membrane periphery in endothelial cells in vitro after treatment with BIA (fig. S9A). We also observed a marked reduction in the BBB tight junction molecule ZO-1 but no difference in levels of Claudin-5 (fig. S9A). BIA decreased levels of CDH5 mRNA in two brain endothelial cell lines, which declined for up to 48 hours following BIA treatment (fig. S9B). BIA also reduced the expression of CDH5 in G34-pCDH GBM cells, with simultaneous decline of *WNT7B* and *S1PR3* expression, suggesting that BIA can modulate these endothelial barrier-related molecules in the tumoral context as well and is not restricted to vascular cells only (fig. S9C). Protein levels of CDH5 reached maximum reduction at 12 hours post-BIA treatment and remained down-regulated for a further 48 hours (fig. S9D).

To understand whether BIA might alter barrier formation properties in brain endothelial cells, we performed trans-endothelial electrical resistance (TEER) analysis of monolayers of HCMEC/D3 cells. Treatment with BIA led to a marked decrease of barrier integrity (Fig. 4B). Moreover, addition of BIA 24 hours after plating endothelial cells completely prevented barrier establishment in two endothelial lines (fig. S9E). These effects occurred from 100 nM to 10 μM BIA (fig. S9F), confirming that BIA can disrupt BBB integrity in vitro.

To confirm that CDH5 is an important factor in modulating the loss of barrier formation in the HCMEC/D3 cells, we electroporated a siRNA against cadherin 5 (siCDH5) sequence to HCMEC/D3 cells and assessed their capacity to form a barrier via TEER (Fig. 4C). Loss of CDH5 decreased the rate of barrier formation in these cells, supporting the notion that loss of barrier formation in brain endothelia due to BIA is, at least in part, because of CDH5 down-regulation.

We next tested the effects of BIA on vascular permeability measuring dextran uptake using an in vitro multicellular BBB spheroid model (*12*, *26*–*28*), which has been shown effective to measure permeability of peptides and chemotherapies. In this experiment, BIA decreased the expression of CDH5 in a dose-dependent manner (Fig. 4, D and F) as shown by IF staining. F-actin was also reduced considerably (Fig. 4, D and G). Incubation of a fluorescent dextran (70 kDa) with the BBB spheroids treated with BIA showed a dose-dependent increase in permeability (Fig. 4, E and H).

To understand whether the effects we observed are a consequence of endothelial cell death, we screened for apoptosis via flow cytometry, which did not show late apoptosis/necrosis at any of the BIA concentrations used in comparison to a cisplatin control (fig. S10A). Cellular adenosine triphosphate (ATP) content was reduced up to 30% in the ~1 to 5 μM BIA range and ~50% and above for HBMECs treated at the same concentrations (fig. S10B), indicating that BIA affects endothelial cell metabolism. Visual assessment of HCMEC/D3 cells treated with BIA did not reveal signs of apoptosis or necrosis but an elongated phenotype with long filipodia (fig. S10C). Cell cycle analysis via flow cytometry showed a slight decrease in proportions of cells in G_1 and G_2/M phases, indicating that BIA affects endothelial cell proliferation but does not induce cell death at the concentrations tested (fig. S10D). Cell counts of endothelial cells treated continuously with BIA showed that cell numbers decreased significantly after 4 days posttreatment (fig. S10E).

BIA targets several kinases in brain endothelium in vitro

BIA is a broadly selective protein kinase inhibitor (*15*, *29*). To elucidate the kinase signaling pathways altered by BIA that could be involved in barrier modulation, we treated HCMEC/D3 cells with BIA and performed phospho-kinase array profiling (Fig. 4, I and J). We observed a decrease of activating phosphorylation in members of the mitogen-activated protein kinase (MAPK) family (p38α, c-Jun N-terminal kinase 1, mitogen- and stress-activated protein kinase 1/2, and extracellular signal–regulated kinase 1/2), SRC family (SRC, YES, and FGR), and transcription factors at activator sites [cAMP response element–binding protein (CREB), signal transducer and activator of transcription 1 (STAT1), STAT2, STAT5a/b, and c-JUN]. The MAPK and SRC pathways are known to control endothelial transcriptional programs through CREB and other transcriptional regulators (*30*–*32*). On the other hand, we observed increased phosphorylation of STAT3 at S727 and Y705 and in p70 S6 kinase, which suggests activation of the Mammalian Target of Rapamycin (mTOR) pathway. Secretome analysis of HCMEC/D3 cells treated with BIA indicates a proinflammatory secretion profile with an increase of cytokines such as tumor necrosis factor–α, interferon-γ, interleukin-17A (IL-17A), IL-6, IL-1β, prolactin, CCL8, and CCL4, among others (fig. S11A); whereas significant down-regulation was seen to occur for CCL2, CCL5, Angiopoitein-2, and CXCL10 (fig. S11B). We confirmed the increased expression of IL-6 and reduction of WNT7A/B by Western blot, which correlated with GSK3b (Ser^9) reduction (fig. S11C). Moreover, we confirmed our phosphokinome array by observing down-regulation of phosphorylation in STAT5A/B, TYK2, p38α, SRC, and CREB upon various BIA doses in endothelial cells (fig. S11D). This correlated with decreased CDH5 expression. Overall, our results indicate that BIA operates at different cellular signaling levels that induce diverse biological changes in brain endothelium, which might be required to induce the endothelial barrier disruption phenotype observed.

BIA increases intratumoral drug accumulation in xenograft models of GBM

To understand whether BIA could also increase permeability in the BTB in the context of GBM in vivo, we implanted patient-derived GBM cells (G30) in nude mice and treated them with BIA and administered sodium fluorescein as indicated in Fig. 5A. Increased accumulation of sodium fluorescein within the tumor was observed after BIA administration, in comparison with untreated controls (Fig. 5B). Analysis of the fluorescent signal showed significant accumulation in the tumor but not in the healthy brain, suggesting that BIA administration promoted intratumoral uptake of sodium fluorescein.

We then interrogated whether BIA treatment could increase the intratumoral accumulation of cisplatin, a nonbrain penetrant

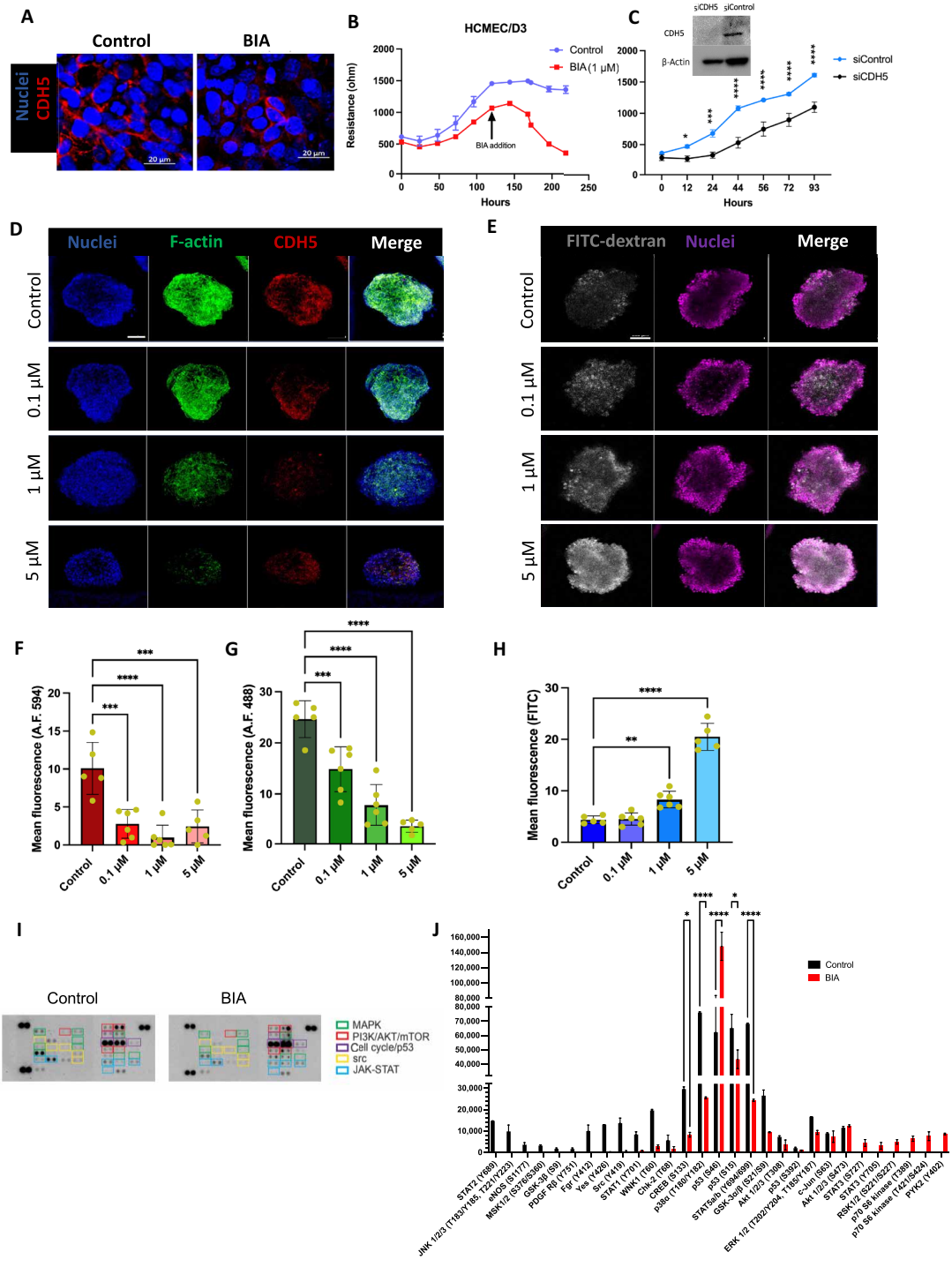

Fig. 4. BIA prevents barrier formation by brain endothelial cells in vitro and increases dextran uptake in a three-dimensional BBB spheroid model. (**A**) IF staining of CDH5 (red) and nuclei (blue) in HCMEC/D3 cells treated with BIA (1 µM, 24 hours). Scale bar, 20 µm. (**B**) TEER values of HCMEC/D3 treated with BIA upon monolayer confluence. Time point of BIA addition is indicated. (**C**) Interference RNA depletion of CDH5 in HCMEC/D3 cells and TEER values of these cells upon ECIS measurement. Western blot for CDH5 depletion confirmation is shown. β-Actin was used as a loading control. (**D**) IF images of BBB spheroids treated with indicated doses of BIA for 72 hours. Staining of F-actin (green), CDH5 (red), and nuclei (blue). Maximal projection intensity is shown from z-stack images (50 µm depth, 20 layers). Scale bar, 100 µm. (**E**) FITC-conjugated dextran (70 kDa) permeability assay in BBB spheroids. Dextran (gray) and nuclei (purple) are shown. Scale bar, 100 µm. Mean fluorescence quantification of (**F**) CDH5, (**G**) Phalloidin and (**H**) FITC-dextran from images in (D) and (E) using the ImageJ software. A.F., Alexa Fluor. Data show mean and SD, $n = 4$ to 5. Ordinary one-way analysis of variance (ANOVA) test. $^{*}P = 0.018$, $^{**}P = 0.0028$, $^{***}P = 0.008$, and $^{****}P < 0.0001$. (**I**) Human phospho-kinase array of HCMEC/D3 cells exposed to 1 µM BIA for 24 hours. Highlighted wells related to indicated pathways. Samples were analyzed in duplicates. (**J**) Quantification of signal by ImageJ of dot blot shown in (I). Mean and SD of duplicates are shown. Two-way ANOVA analysis was performed. $^{**}P = 0.0015$, $^{***}P = 0.005$, and $^{****}P < 0.0001$.

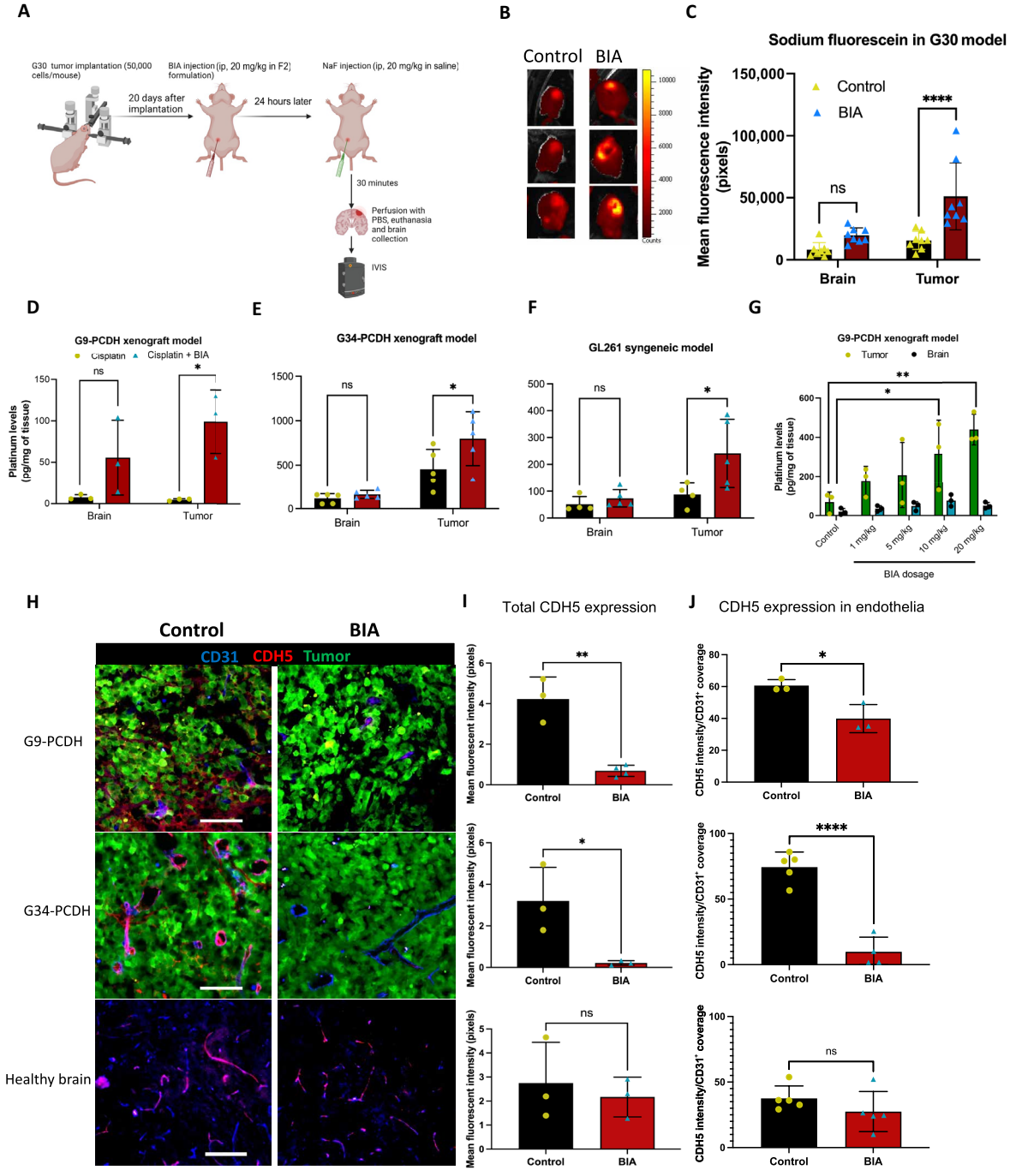

Fig. 5. Systemic administration of BIA increases the selective uptake of sodium fluorescein and platinum chemotherapy in GBM murine tumors. (**A**) Workflow schematic of BIA administration and subsequent injection of Sodium Fluorescein (NaF) for BTB permeability assessment. Panel figure was generated using Biorender.com. (**B**) In vivo imaging system (IVIS) pictures of G30 tumor–bearing brains from mice injected with BIA and NaF as shown in (A). (**C**) Quantification of image intensity was performed with ImageJ (Fiji). Mean and SD are shown, $n = 7$ to 8. Unpaired t test for statistical significance, $^{****}P = 0.0024$. (**D**) Platinum quantification via ICP-MS of brain and tumor tissue from tumor-bearing mice injected with cisplatin in G9-PCDH, (**E**) G34-PCDH, and (**F**) GL-261 murine models. Cisplatin (5 mg/kg) was administered 24 hours after BIA injection. Mean and SD are shown, $n = 3$ to 5 per group. Two-way ANOVA statistical analysis was performed, $^{*}P < 0.05$. (**G**) Platinum quantification via ICP-MS of tumor and brain tissue of a G9-PCDH tumor–bearing xenograft model administered with increasing BIA doses. Mean and SD are shown, $n = 3$ per group. Two-way ANOVA test, $^{*}P = 0.0177$ and $^{**}P = 0.0016$. (**H**) Confocal IF imaging from frozen and sectioned brain tissue from G9-PCDH and G34-PCDH xenograft murine models, 24 hours after injection with BIA (20 mg/kg). CDH5 was stained in tumor and healthy brain tissue with Alexa Fluor 594 and blood vessels with anti-CD31 and Alexa Fluor 405. GBM cells are prelabeled with GFP. Images shown at 20×, with scale bars at 100 μm, accordingly. (**I**) Total CDH5 fluorescence quantification (Alexa Fluor 594) and (**J**) CDH5 coverage in $CD31^{+}$ vessels from experiment in (E) using ImageJ (Fiji). Mean and SD are shown. Unpaired t test ($n = 3$ per group). $^{****}P < 0.0001$, $^{**}P = 0.0013$, and $^{*}P = 0.0334$. ns, not significant.

chemotherapy. For this, we injected cisplatin (5 mg/kg) and allowed circulation in the system for 5 hours. We collected and processed the tissue downstream (see Materials and Methods) for inductively coupled mass spectrometry (ICP-MS) analysis–based platinum quantification (fig. S12A). Pretreatment with BIA permitted significant cisplatin intratumoral accumulation in patient-derived (Fig. 5, D and E) and syngeneic murine GBM tumors (Fig. 5F). No significant difference of uptake was seen in contralateral healthy brain regions, indicating that BIA acts selectively in the tumor but not in the brain. Moreover, no difference in platinum accumulation was seen in peripheral tissues such as the heart or liver, thereby supporting the notion that BIA selectively increases cisplatin uptake in tumor but not healthy tissue (fig. S12B). Tumor sizes between control and BIA-treated groups before administration were comparable by IF imaging for the patient-derived and syngeneic models (fig. S12, C to E).

Further studies showed that the uptake of cisplatin is dependent on the dose of BIA (Fig. 5G). To test possible mechanisms of how BIA operates in augmenting drug accumulation in tumors, we treated GBM cells (fig. S12F) and brain endothelial cells (fig. S12G) with BIA and cisplatin simultaneously. In either case, we did not observe any advantage in drug accumulation due to BIA addition, suggesting that direct cellular internalization is not a mechanism of operation for BIA. Treatment of endothelial cells with BIA did not show any changes of protein levels of CAV1 or MFSD2A (fig. S12H), important molecular actors in endocytosis and transcytosis in the BBB.

Next, we evaluated CDH5 expression in our patient-derived xenograft GBM models and its potential alterations upon BIA treatment. Administration of BIA showed a notable decrease of CDH5 in the whole section and in $CD31^+$ endothelial cells 24 hours after treatment (Fig. 5, H to J). On the other hand, we did not observe significant changes in expression of CDH5 in contralateral healthy brain regions, which is consistent with the observation that increased drug delivery effects due to BIA are tumor associated endothelium specific. In addition, we assessed the expression of ZO-1 and Claudin-5 in these tissues. We observed mild reductions of ZO-1 expression as well but no visible differences in Claudin-5 staining (fig. S12I).

To identify any possible effects of BIA treatment on additional components of the BBB/BTB endothelium or basement membrane, we stained our G9-pCDH xenograft model for the endothelium (CD31) (fig. S13A) and for pan-laminin (fig. S13B) and COL1A1 (fig. S13C). We did not observe morphological differences on the $CD31^+$ blood vessels nor changes of signal intensity of COL1A1; however, we did find a marked decrease of laminin staining on these vessels. This indicates that BIA might alter the expression of additional elements of the BTB besides CDH5 in the endothelial compartment, which supports the notion that BIA can modulate the BTB transcriptome at multiple molecular layers.

We performed IF on additional GBM endothelium–enriched transcripts that we identified in two patient-derived xenograft models. We observed a considerable reduction at the endothelium of ACVRL1 staining (fig. S14A) upon BIA administration above control. We also saw a mild decrease of PDGFR-β^+ cells alongside CD31-expressing vessels (fig. S14C) and endoglin (fig. S14D) in the vascular regions of G9-PCDH and, to a greater extent, in G34-PCDH. We observed considerable down-regulation of Endothelial Cell Adhesion Molecule (ESAM) after BIA treatment (fig. S14B) in the G34-pCDH model but not G9-pCDH, which might reflect intermodel variability of response to BIA. Collectively, our data provide evidence that BIA selectively targets the tumoral vasculature at the BTB, which down-regulates CDH5 expression and other GBM endothelium–enriched transcripts, disrupting tight junction formation and increasing accumulation of chemotherapy in murine GBM tumors.

BIA potentiates cisplatin cytotoxicity by fostering its DNA damage capacity

Before animal efficacy studies, we also asked whether BIA and cisplatin in combination could also show a therapeutic advantage than administration of either agent alone. Several studies have shown cytotoxic synergy of small-molecule kinase inhibitors in combination with cisplatin in cancer (*33*–*35*). Accordingly, we cultured a panel of patient-derived GBM neurospheres and treated with BIA and cisplatin combination, with single-treatment groups as controls (Fig. 6A). Using a cell viability assay, we observed that combination of BIA markedly increased the cytotoxic effects of cisplatin alone. The most significant combinatorial effects were observed at cisplatin concentrations of 1 μM and below. BIA single-treatment controls only mildly reduced cellular ATP production. In accordance, the BIA/cisplatin combination decreased the neurosphere formation capacity and growth of G9 and G34 cells (fig. S15, A to D). To identify potential synergistic interactions between BIA and cisplatin, we used SynergyFinder 3.0 software. BIA potentiated cisplatin toxicity (overall δ-score = 8.24), at a concentration of 2.5 μM and below (Fig. 6B). We also identified a high likelihood of synergy (highlighted area, δ-scores > 10) at the lower doses for cisplatin (~0.6 to 2.5 μM) in combination with all tested BIA doses (Fig. 6C). At the upper cisplatin dose ranges, its interaction with BIA remained nonsynergistic. Thus, cisplatin and BIA in combination show synergistic antiglioma cytotoxic effects.

Next, we assessed the DNA damage levels of the BIA/cisplatin combination by IF imaging of γH2AX nuclear foci. This showed that the BIA/cisplatin combination significantly augmented the frequency of γH2AX foci in the nucleus of GBM cells above single-treatment and nontreated controls (Fig. 6, D and E). This increase in γH2AX events in the BIA/cisplatin combination was also observed by flow cytometry, which correlated with loss of cell cycle progression (fig. S15, E and F). We evaluated the phosphorylation and protein levels of CHK1, an important regulator of the DNA damage response during cisplatin exposure (*36*). Simultaneous exposure of BIA and cisplatin reduced the expression of CHK1 and its activation (Ser^{345}) greater than single-treatment controls. In turn, γH2AX levels were induced upon this combination (Fig. 6F). Given the strong depletion of CHK1 activity, we performed small interfering RNA (siRNA)–dependent knockdown in our GBM cell lines. Use of siCHK1 increased the susceptibility of these cells to cisplatin titrations, mainly at concentrations below 1 μM cisplatin (fig. S15G), supporting the notion that targeting of CHK1 is an important factor in the BIA-induced potentiation of cisplatin cytotoxicity.

BIA enhances cisplatin preclinical efficacy in patient-derived GBM xenografts

Last, we investigated whether BIA and cisplatin combination regimens could provide a therapeutic effect in our intracranial GBM murine models. We proceeded with a dose regime of BIA preadministration 24 hours before cisplatin injection at 5 mg/kg to promote and maintain increased platinum delivery (Fig. 7A). The BIA and cisplatin

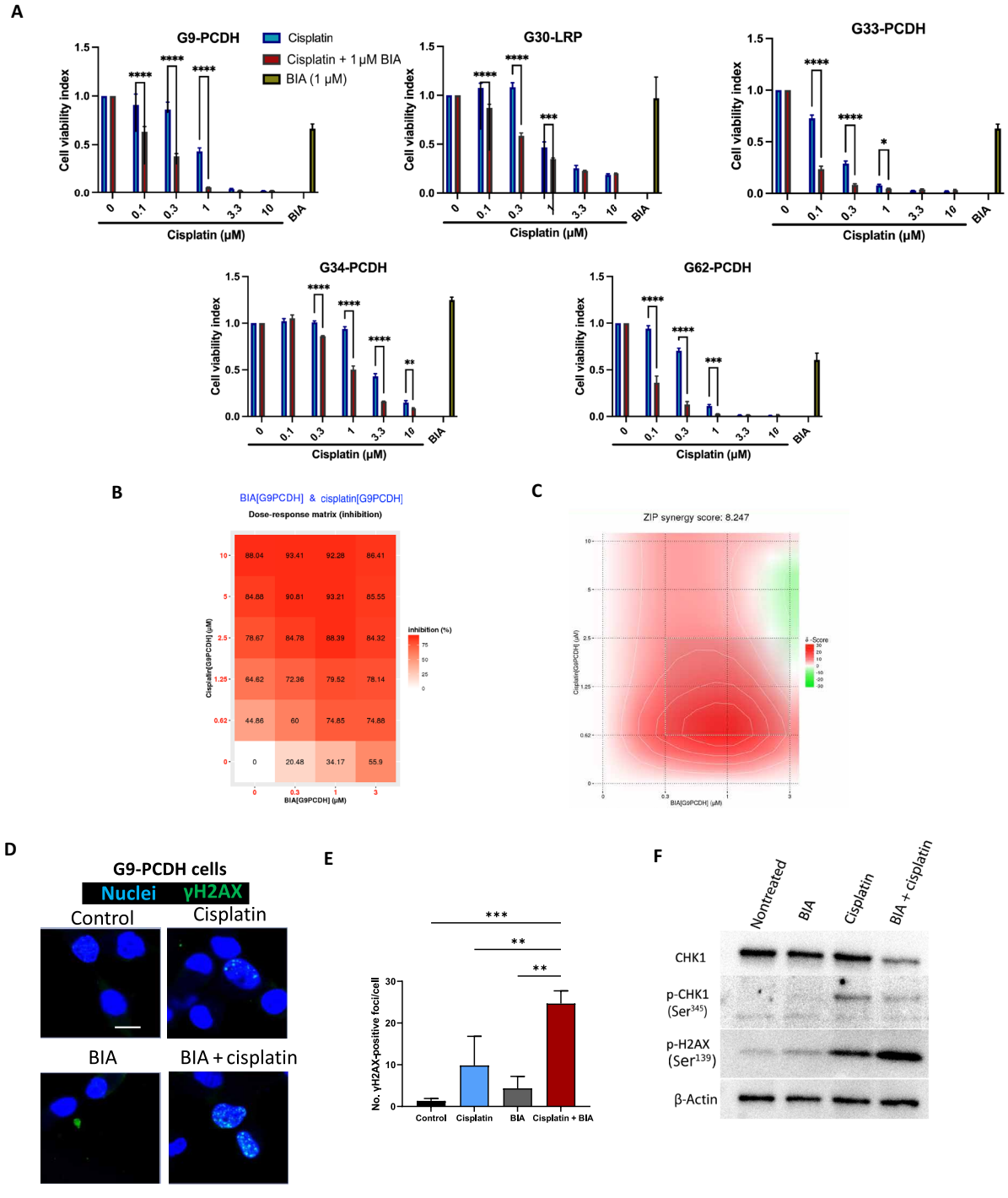

Fig. 6. BIA potentiates platinum-based cytotoxicity by targeting DNA repair pathways in patient-derived GBM cells. (**A**) GBM cell viability assay (ATP-based) using Cell-Titer Glo 3D of BIA and cisplatin combination treatment. Cisplatin doses are indicated in the *x* axis, and BIA remained at a constant concentration of 1 μM. Cells were treated for 5 days and analyzed using a plate reader for luminescence quantification. Mean and SD are shown, $n = 3$ per group. (**B**) Dose-response matrix showing inhibition percentage of BIA and cisplatin combinations at various concentrations using SynergyFinder 3.0. G9-PCDH cells were treated and viability analyzed as indicated in the cell viability assay section (see Materials and Methods). (**C**) ZIP method synergy score of BIA and cisplatin combinations. The overall average δ-score is indicated on top of the chart. The dose combinations showing an increased likelihood of synergy are highlighted. (**D**) IF staining of γH2AX (Alexa Fluor 647) in G9-PCDH cells treated with 1 μM cisplatin and/or BIA, for 72 hours. Nuclei were stained using Hoechst 33342. Representative image of five pictures per condition. Pictures taken at 40×. Scale bar, 20 μm. (**E**) Quantification of γH2AX foci from (B) using ImageJ. (**F**) Western blot of G9-PCDH cells treated with 1 μM cisplatin and/or BIA, for 72 hours, probing for the phospho-CHK1, CHK1, and phospho-H2AX proteins. GAPDH was used as loading control and cleaved poly(adenosine diphosphate–ribose) polymerase as a cell death marker. Representative image from triplicate experiments. $^{*}P = 0.028$, $^{**}P < 0.01$, $^{***}P < 0.001$, and $^{****}P < 0.0001$.

combination regimens prolonged the survival of tumor-bearing mice significantly ($P = 0.0052$) over the single-treatment and control arms, indicating efficacious results by this approach (Fig. 7B).

BIA is highly hydrophobic, making it difficult to dissolve in physiological solutions, which limits its clinical translation. To address this, we used PPRX-1701, a formulation of BIA, designed for improved in vivo delivery (*37*), which inhibits GSK3 as indicated by a G9-TCF cell line reporter (fig. S16, A and B). Previously, we have shown that PPRX-1701 is not toxic when administered systemically in C57/BL6 mice, as shown by liver and spleen histology (*37*). We implanted a second patient-derived GBM xenograft model (Fig. 7C) and performed systemic preadministrations of PPRX-1701 before cisplatin injections. Combination of PPRX-1701 with cisplatin was also more efficacious in comparison with vehicle control plus cisplatin, PPRX-1701 alone, and nontreated controls ($P = 0.0016$) (Fig. 7D). Assessment of DNA damage by γH2AX staining indicated that PPRX-1701 enhanced the genotoxicity of cisplatin, correlating with the extended survival observed (Fig. 7, E and F).

Together, our data highlight potential molecular targets associated to the BTB in GBM. In addition, we demonstrated that BIA exerts preclinical efficacy in GBM murine models through its dual capacity to selectively target transcriptional programs of the BTB, promoting intratumoral drug delivery and by showing cytotoxic synergistic effects with DNA-damaging chemotherapy (Fig. 7G).

DISCUSSION

Effective drug delivery remains a major challenge for the treatment of brain tumors. Here, we have identified a network of genes associated with the BTB in GBM and have demonstrated the dual functionality of the indirubin derivative, BIA, to increase intratumoral drug delivery by targeting the BTB-associated gene network and enhance chemotherapy cytotoxicity via DNA repair machinery modulation. Our work should provide grounds to establish further studies for progressing BTB-targeting approaches toward clinical application.

We used an in silico strategy from bulk RNA-seq datasets, based on GBM-associated vascular markers identified by Dusart *et al.* (*17*), to identify a set of 12 genes (GBM endothelium–enriched transcripts) with elevated regional expression within the tumoral endothelium in GBM. We performed this analysis by identifying gene coexpression with known endothelial markers *PECAM1* and *VWF*, as well as with angiogenic and tumoral vasculature reference transcripts *CD34* and *CLEC14A*. CD34 is also a well-known marker of progenitor bone marrow cells, some with reported potential to microglial differentiation (*38*, *39*). Moreover, albeit unfrequently, GBM tumor cells have reportedly presented CD34 positivity (*40*). In contrast, CD34 expression has been consistently reported in progenitor endothelial cells and tip-angiogenic cells (*41*–*43*), being widely used as an endothelial marker when used simultaneously with PECAM1 and/or VWF canonical markers. *CLEC14A* has been implicated in tumoral angiogenesis (*44*) and is used as a tumor endothelial marker (*45*), undergoing preclinical applications such as CLEC14A-specific Chimeric Antigen Recombinant T-cell (CAR-T) targeting (*46*). Thus, we proceeded using these markers for tumoral vasculature screening.

We performed spatial transcriptomic data reanalysis (*20*) of *CDH5* and the other identified GBM endothelium–enriched transcripts. This showed high spatially clustered expression of these genes in perivascular regions of GBM clinical samples, suggesting a functional relevance for this disease. Most of the GBM endothelium–enriched transcripts have been associated with angiogenesis and blood vessel recruitment, especially *ACVRL1*, *CD93*, *ENG*, *FLT4* (VEGFR3), and *PDGFRB*. Previous studies (*47*) have indicated the coexpression of *ACVRL1*, *CDH5*, *CLEC14A*, *PECAM1*, *ENG*, *GRP4*, *ROBO4*, and *PCDH12* in the tumor-associated endothelium in several solid tumor types, including GBM. This gene set has been related to vascular development, blood vessel morphogenesis, and tumor angiogenesis processes. These biological processes have also been identified in endothelium of primary GBM specimens (*48*, *49*). The mentioned reports support our findings and indicate the functional relevance of these genes in the vascular developmental processes of the BTB in GBM. It is of importance to note that the identified GBM endothelium–enriched transcripts also have functional roles in other non-endothelial compartments. For instance, PDGFR-β is a well-known pericyte marker, although it also has been reported to have a role in endothelial angiogenesis via the Talin1/FAK axis (*50*). ACVRL1 deficiency promotes arteriovenous vascular malformations due to reduced mural cell coverage upon VEGF stimulation (*51*). Mutations in ACVRL1 and ENG promote the incidence of hereditary hemorrhagic telangiectasia, which present increased bleeding and vascular aberrations (*52*). ROBO4, a member of the ROBO family of receptors for Slit ligands, has been shown to modulate the BTB permeability (*53*) but also guides and modulates angiogenesis for vascular network structuring (*54*). Moreover, ROBO4 performs as a guide molecule for cortical neuron development (*55*). In a similar manner, PCDH12 is required for neuronal timely differentiation and migration upon cortical development (*56*). Yet, PCDH12 expression has also been reported in endothelia (*57*). These GBM endothelial transcripts have pleiotropic functions, and what are the consequences of their targeting with BIA in other non-endothelial compartments remains to be studied. To confirm that these transcripts are relevant for GBM vascular biology, we screened their single-cell expression in the Wälchli *et al.* (*18*) brain vasculature atlas. The analysis confirmed that the 12 GBM endothelial–enriched transcripts are mostly expressed in endothelial and perivascular cells, that these are up-regulated in GBM vasculature above healthy brain tissue and other malignancies, and that their expression can vary across endothelial subsets, tumors, and patients with GBM. In the context of GBM vasculature, our work links the modulation of these GBM endothelium–enriched transcripts and vascular pathways to alter BTB permeability for improved drug delivery in tumors. Future work by us would involve functional studies on these molecules for deeper understanding of their involvement in BTB biology.

Our screening led us to investigate CDH5 (VE-cadherin) as a central element in the tumoral-associated vascular transcriptome. CDH5 is fundamental for endothelial barrier integrity, but its role in BTB permeability is not fully understood. Transcriptional and IF studies showed prominent expression of CDH5 in vascular regions of GBM clinical samples, and its expression was correlated with endothelial markers above nontumor cortex when analyzed by spatial and single-cell transcriptomics. Genetic depletion of CDH5 caused a delay in barrier formation capacities in brain endothelial cells as measured by trans-endothelial resistance, and its down-regulation strongly correlated with increased drug accumulation after BIA injection in our GBM murine models. It was of interest to us that

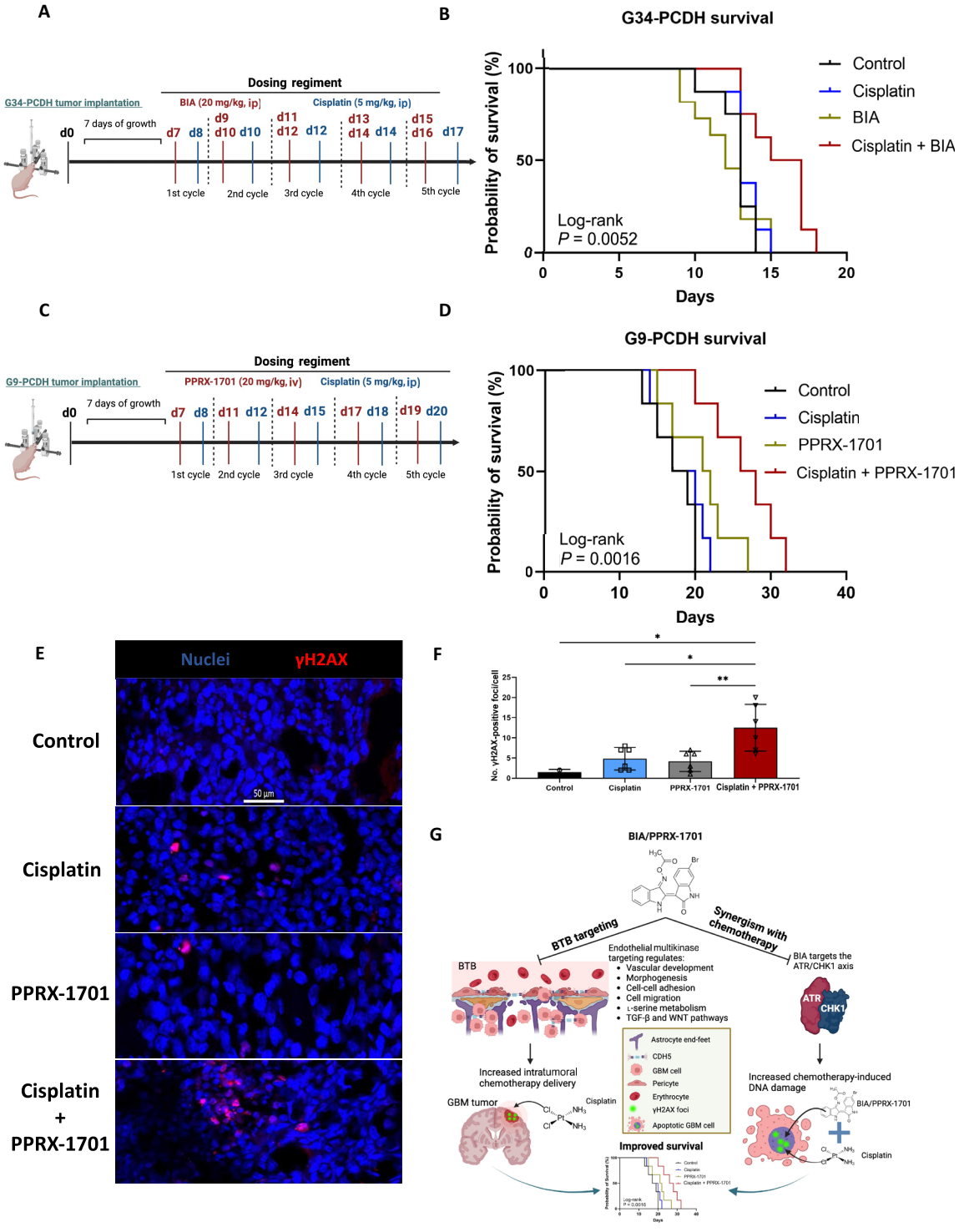

Fig. 7. Systemic administration of BIA or PPRX-1701 in combination with cisplatin treatment shows enhanced preclinical efficacy in murine GBM models. (**A** and **C**) Diagrams of the experimental design for G34-PCDH and G9-PCDH xenograft efficacy studies using BIA/PPRX-1701 and cisplatin combinations. Both panel figures were generated using Biorender.com. (**B**) Efficacy studies of G34-PCDH xenograft using BIA and (**D**) PPRX-1701 in combination with cisplatin. For PPRX-1701 studies, empty nanoparticles were used as controls and in combination with cisplatin. $N = 8$ per group. Log-rank test analysis for statistical significance. (**E**) Confocal IF imaging of γH2AX (Alexa Fluor 647, red) nuclear foci from tumor tissue collected from study (D). Nuclei were stained with Hoechst 33342 (blue). Representative pictures taken at 20×. Scale bar, 50 µm. (**F**) Quantification of γH2AX foci from (E) using ImageJ, $n = 6$ per group. Ordinary One-way ANOVA was performed for statistical evaluation. $^{*}P = 0.01$ and $^{**}P = 0.0086$. (**G**) Schematic of proposed model of BIA/PPRX-1701 mechanism of action and its effects in GBM tumor drug delivery and antioncogenicity. Figure panel was generated using Biorender.com.

CDH5 was not only present in endothelium but also highly expressed in other cell types negative for CD31, a universal marker of blood vessels. This correlated with our spatial transcriptomic data showing spatial distribution of CDH5 in endothelium and other cell clusters. CDH5 colocalization with CD31 was mainly observed in smaller vessels, but not hyperplastic vessels, which is an interesting biological effect that we will pursue to address in future studies that will involve multiplex analysis. Several reports have shown that GBM tumor cells engage in vascular mimicry to facilitate blood vessel formation that permits tumoral migration and invasion (*58*). CDH5 has been associated with enabling vascular mimicry capacity in GSCs (*25*), permitting formation of vascular-like structures that supply with nutrients and facilitate anti-angiogenic therapy resistance. CDH5 enrichment has been associated with increased immune infiltration and positive prognosis in other solid tumors, such as bladder cancer (*59*), thus indicating potential benefits for endothelial CDH5 targeting in combination with immunotherapies. Our data using Pearson correlation for $CD31^+$ and CDH5 coexpression suggested that GBM vasculature expresses CDH5 across the tumor in a similar manner, and this expression is significantly elevated compared to $CDH5^+$ tumor cells, supporting the hypothesis that CDH5 is a central element in the vasculature comprising the BTB.

Our findings show that BIA down-regulates CDH5 gene expression and other GBM endothelium–enriched transcripts such as ACVRL1 and ENG, in endothelial cells in vitro (Fig. 3D) and in vascular and tumoral compartments in vivo (Fig. 5H and figs. S10 and S11). We also observed decreased expression of ENG, ESA, ACVRL1, PDGFR-β, and laminin alongside $CD31^+$ vessels. Current efforts are taken to elucidate the effects of loss of PDGFR-β in the perivasculature and laminin at the basal membrane for drug delivery purposes. On the other hand, our bulk RNA-seq studies lead to identify altered expression levels of genes involved in TGF-β and Wingless-Type (WNT) signaling, fundamental pathways in BBB formation and stability. The TGF-β pathway maintains BBB integrity through cross-talk with oligodendrocytes, pericytes, and endothelial cells (*60, 61*). We observed down-regulation of several members of this pathway. The WNT/β-catenin pathway is fundamental for brain and retinal barrier genesis and maintenance, especially the Norrin/WNT7A/B axis (*62, 63*). We observed a decrease of *WNT7B* and WNT ligand receptors *FZD4* and *FZD7*, with simultaneous increase of expression of *WNT4*, *WNT10A*, and *WNT11* ligands. In addition, transcriptional alteration of genes involved in angiogenesis (i.e., *ANGPT2*, *ENG*, and *ANG*) and BTB permeability (*S1PR1* and *S1PR3*) was also seen. As such, CDH5 down-regulation and alteration of other BBB integrity components might work together to contribute to the BTB permeability modulation exerted by BIA. Future work by our team will focus on functional interrogation of the potential roles of CDH5 and other GBM endothelium–enriched transcripts in the tumor-associated vasculature and their relevance in the permeability of the BTB for drug delivery purposes.

Our current understanding of BTB biology has relied mainly on in vivo models of GBM and patient data. However, several in vitro models are under development to study the molecular and pathophysiological heterogeneity of the BTB in brain tumors (*64*–*66*). These models involve utilization of lab-on-a-chip microfluidic models of perivascular, endothelial, and tumoral coculture (*67*–*70*) under blood flow–simulating conditions. These models will also aid in screening other BTB-modulating compounds and their mechanisms of action, allowing the identification of additional therapeutic options for BTB targeting.

The BTB shows both inter- and intratumoral heterogeneity, with some regions maintaining healthy BBB characteristics, preventing efficacious drug intratumoral accumulation (*4*, *6*). Spatial single-cell studies must be pursued to elucidate BTB heterogeneity for identification of drug biodistribution modulators in GBM. These could be coupled with mass spectrometry–based tools, such as matrix-assisted laser desorption ionization–mass spectrometry imaging (*71*) and laser ablation ICP-MS (*72*), which would be useful to inform on drug uptake in a regional fashion.

The administration of BIA to tumor-bearing xenograft and syngeneic mice enhanced the accumulation of cisplatin and sodium fluorescein in the brain tumor tissue but not the healthy brain. The specificity of this effect toward tumorigenic regions remains under study by us. It is likely that BIA, being a small-molecule kinase inhibitor, targets cells with elevated kinase signaling activity, such as the case of angiogenic/proliferative endothelium, but spares slow cycling/quiescent cells that constitute the nontumorigenic brain vascular networks. Vascular development and motility programs are active in angiogenic endothelial cells, and the multitargeting quality of BIA can dysregulate multiple elements involved in these pathways. We also observed inactivation by dephosphorylation of the endothelial nitric oxide synthase, important blood pressure regulator, and the p38α/CREB axis, which can control gene expression of CDH5 and other genes important to endothelial biology. The p53 tumor suppressor protein also showed an increase of activating phosphorylation sites (S46) and loss of phosphorylation modulating proapoptotic (S392) and gene regulation (S15) activities. The p53 factor has been involved in modulating endothelial vasodilation and functions in vascular remodeling (*73*–*75*). On the other hand, BIA promoted the expression of genes relevant to L-serine metabolism and amino acid transport processes. L-serine has been reported to improve cerebral blood flow, which provides neuroprotection during CNS disease (*76*). In this regard, normalized blood flow can also promote drug accumulation in solid tumors (*77, 78*). The mTORC1 complex is an important amino acid sensor, which regulates protein synthesis and energy modulation. We observed an increased phosphorylation of p70 S6 kinase, a downstream target of the mTORC1 pathway. This is consistent with the observation that BIA promotes expression of genes related to amino acid transport and synthesis. This could be a result of indirubin-derived metabolic secondary effects. Future work focusing on the potential role of the mTOR pathway in GBM vascular permeability should be performed to confirm and address the therapeutic relevance of such observations.

Simultaneous exposure to BIA and cisplatin had a synergistic killing effect in GSC-like cells. This correlated with increased DNA damage and CHK1 inhibition. Other studies have shown that indirubin derivatives induce DNA damage in HCT-116 cancer cells (*79*). However, the present work reveals a previously unidentified applicability of BIA, and potentially other indirubins, in combinatorial regimens to synergize with DNA-damaging chemotherapy. Administration of BIA or PPRX-1701 nanoparticles, which we have previously shown to be safe at 20 mg/kg intravenously and reach murine brain (*37*), followed by cisplatin after 24 hours, caused a significant extension of survival of two different GBM xenograft models. Most likely, this improved preclinical efficacy stems from the increased platinum delivery intratumorally and the additive cytotoxicity exerted by both agents. Given this finding, other DNA-damaging chemotherapeutics should be screened in combination

with BIA to identify alternative drug candidates that would benefit from the increased accumulation and BIA antineoplastic synergism in GBM treatment. The mechanism of how BIA down-regulates CHK1 expression at the protein level and what alternative therapeutic modalities (i.e., TMZ and radiotherapy) will benefit from BIA simultaneous administration remain in an ongoing study by us. There is no evidence available to us yet that the down-regulation of CDH5 and the GBM-associated transcripts and vascular permeability due to BIA is mechanistically related to this antiglioma synergistic effect in combination with cisplatin, but rather independent pathways targeted by BIA simultaneously. Our Western blot and siRNA experiments link this to BIA modulation of CHK1, which potentiated cisplatin cytotoxic effects in GSCs.

Clinical studies performed with indirubins are very limited. Oral administration of indirubin has been investigated for the treatment of ulcerative colitis and inflammatory bowel disease, where doses ranged from 0.5 to 2.0 g daily (*80, 81*), and for chronic myeloid leukemia, with an intravenous administration of 100 mg daily (*82*). No synthetic indirubin, including BIA, has been tested in the clinic to date. Using basic allometric scaling calculation (*83*), we infer that an approximate of 113 mg of BIA would be necessary for a 70-kg person to present similar effects as seen with a 20 mg/kg–dose preclinically. Hence, the preclinical dosing we present here has the potential to be directly translated into clinical trials using BIA for GBM management.

Other strategies to improve drug delivery in GBM involve vascular normalization (*84*–*86*), using bevacizumab (*87*), and focused ultrasound for transient disruption of the BBB (*8*), among other approaches (*88*). Some of these methods are restrained by dose-limiting toxicity concerns. In the case of BIA, further challenges would involve the identification of its optimal clinical dose to achieve maximal delivery of a coadministered therapeutic, and this should be performed in parallel with metabolic imaging methods, such as magnetic resonance (MR) spectroscopy, to assess cotreatment internalization dynamics (*88*). Successful clinical evaluation of drug delivery would accelerate the translation of BIA into further clinical trials in combination with additional antineoplastic agents.

Together, our work reveals novel molecular markers of the BTB, which in future studies should be functionally characterized to understand their role in the biology of the BTB-GBM interaction. The identification of BIA as a selective regulator of BTB permeability for improved drug delivery and potentiating agent of DNA-damaging chemotherapy supports the use of BIA in further preclinical and clinical studies of GBM. Primarily, further research should be pursued on screening for non-BBB penetrant chemotherapies and biologicals that would benefit from higher intratumoral internalization in combination with BIA, such as clinically tested small-molecule inhibitors, DNA-damaging chemotherapies, and therapeutic antibodies. Experimental assessments whether BIA can also potentiate alternative drug internalization–promoting strategies now tested in the clinic, such as focused ultrasound or vascular normalization, to maximize pharmaceutical intratumoral accumulation would be considerably relevant.

MATERIALS AND METHODS

GBM clinical specimens

Archived brain tumor tissues [formalin-fixed paraffin-embedded (FFPE) samples] are available via an Institutional Review Board (IRB) approved protocol (IRB #816619) from the Lifespan Rhode Island Hospital IRB. All samples were from patients who preoperatively consented to use their tissues via an informed consent process. This includes archived slides, as well as FFPE tissue samples for molecular analysis. Pathology confirmed the presence of GBM tumor in the specimens.

GBM endothelium–enriched transcript in silico screening

To identify genes related to BTB function, we initiated an in silico–based approach by accessing GBM clinical specimen bulk RNA-seq data from The Cancer Genome Atlas via the cBio portal for Cancer Genomics (https://cbioportal.org/). We initiated a correlation analysis of genes coexpressed with endothelial markers PECAM-1 (CD31), VWF, CLEC14A, and CD34, previously identified as useful markers of GBM vasculature by Dusart *et al.* (*17*). A selection of top 50 genes (Spearman's rank correlation) commonly observed in three of the four markers was done and interrogated their expression levels in GBM tumors in comparison to healthy brain by using the GlioVIS portal (http://gliovis.bioinfo.cnio.es/) by visualizing the Rembrandt study (*89*). Those genes significantly elevated in the tumor over the healthy brain were selected as candidate GBM vascular–associated targets due to their possible relevance in GBM. Then, the regional expression of these selected genes in GBM was assessed by using the IVY GAP dataset (https://glioblastoma.alleninstitute.org/) visualized in the GlioVIS portal. Using this tool, we further selected genes with increased expression in microvascular proliferative regions, which are associated with the vasculature in tumors. Those genes with significantly enriched expression at the microvascular proliferation regions were denominated as the GBM endothelial–associated transcripts. All graphs of GlioVIS and cBio portal datasets were generated in the corresponding websites, and pairwise *t* tests were performed for statistical significance test.

GO analysis

For GO analyses, we used the EnrichR (https://maayanlab.cloud/Enrichr/) website, generated by the Ma'ayan's lab (*90*–*92*). We used the GO Biological Process 2023 visualization tool to identify biological processes of the identified gene sets. The Appyters notebook (*93*) linked to EnrichR was used for graphic visualization.

Gene interaction network analysis and gene set clustering

Gene sets were submitted to the STRING [https://string-db.org/ (*94*)]. Scores were set to medium interaction (0.4). For interaction analysis of the genes targeted by BIA, we selected genes up-regulated and down-regulated by BIA equals or above twofold change ($\log_2$). Only genes that presented interaction were associated by a 4-kmeans clustering. Gene sets comprising each cluster were submitted to GO analysis (using EnrichR as mentioned above) and ranked by *P* value significance. The most significant pathway by this method is indicated by color code in each cluster.

Spatial transcriptomic dataset analysis and clustering methods

Here, four specific datasets of a larger set of 28 were focused on data available from (*20*) and the dataset that was deposited in Datadryad (https://doi.org/10.5061/dryad.h70rxwdmj) by the authors. These datasets were collected from patients with tumor and cortex control samples. To analyze the effect of CDH5, we started clustering our spatial dataset and visualizing the gene expression

spot information with spatial dimensions using the SPATA2 package in R-studio (*95*) (https://github.com/theMILOlab/SPATA2). In addition, using the Seurat package (v5.0.0) in R (v4.2.2), the spatial transcriptomic data were processed in several steps. Initially, the data were loaded and preprocessed, followed by normalization using the log normalization method. Variable features were identified, and the data were scaled accordingly. Principal components analysis (PCA) was then applied to reduce the dimensionality of the dataset, with emphasis placed on the top 20 principal components for subsequent cluster and neighbor analysis based on PCA dimensions. The data were visualized in two dimensions using Uniform Manifold Approximation and Projection (UMAP). The tumor and cortex control datasets were merged into a single Seurat object using the merge function (Seurat::merge()). Subsequently, the spatial layers were processed to facilitate visualization of the data in two dimensions. Gene expression patterns were analyzed using the same dimension reduction plot, and expression levels were assessed with violin plots within each cluster identified by the Seurat algorithm.

Spatial GO analysis

The GO analysis used a cluster-based methodology conducted in R, with clusters determined by the Seurat algorithm. Initially, differential expression analysis was conducted in Seurat to identify genes and their associated cluster information within the samples (Seurat::FindAllMarkers()). Subsequently, genes were individually grouped on the basis of their clusters, and GO analysis was performed using the enrichGO function in the clusterProfiler package (https://bioconductor.org/packages/release/bioc/html/clusterProfiler.html). A reference genome-wide annotation for human, primarily using mapping via Entrez Gene identifiers, was obtained from the org.Hs.eg.db package within the Bioconductor library and converted into a data frame. Visualization of the GO data was accomplished using the GOplot package (GOplot::GoBubble()). For optimal visualization, only the cluster containing CDH5 was selected and depicted in the bubble plot.

Spatial pathway analysis

Pathway analysis was conducted using a gene-based approach, where signature genes corresponding to each pathway were sourced from the Molecular Signatures Database (MsigDB; https://www.gsea-msigdb.org/gsea/msigdb/human/genesets.jsp). Specifically, our focus was on the WNT pathway, VEGF angiogenesis pathway, and TGF-β pathway, with gene extraction performed using the msigdb package (https://bioconductor.org/packages/release/data/experiment/html/msigdb.html). These pathways are categorized within the Curated Gene Sets collection (C2 gene sets) under the Biocarta subcollection. The expression patterns of individual genes derived from this methodology were visualized using the FeaturePlot function in R, enabling two-dimensional visualization.

Visualization of identified GBM endothelium–enriched transcripts in GBM endothelium using single-cell RNA-seq datasets

Using the publicly available websites (https://waelchli-lab-human-brain-vasculature-atlas.ethz.ch and https://brain-vasc.cells.ucsc.edu) from Wälchli *et al.* (*18*), we visualized our identified GBM endothelial–enriched genes by visualizing gene expression of FACS-sorted endothelial and unsorted GBM tumor cells.

Mice

Female Nu/Nu mice (Envigo) and C57/BL6 (Charles River Laboratories) aged 8 weeks were used for in vivo experiments. All our procedures followed the guidelines by the Institutional Animal Care and Use Committee with support of the Center for Animal Resources and Education at Brown University: Preclinical studies on brain cancer, no. 24-09-0004.

Cell lines

Glioma stem cell–like cell lines G9-PCDH, G34-PCDH, G33-PCDH, G62-PCDH, and G30-LRP were obtained and cultured as previously described (*12, 37, 96*). Briefly, cells were grown as neurospheres using neurobasal medium (Gibco) supplemented with human recombinant epidermal growth factor (20 ng/ml; Peprotech), human recombinant fibroblast growth factor (20 ng/ml; Peprotech), 2% B-27 supplement (Thermo Fisher Scientific), 0.1% GlutaMax (Thermo Fisher Scientific), and 0.1% penicillin/streptomycin (Thermo Fisher Scientific). Cells were left to grow at least overnight for sphere formation. For single-cell dissociation, Accutase (Gibco) was used for 5 min at 37°C. For culturing GL261-Luc2 cells, we used 10% fetal bovine serum (Gibco), with 0.1% GlutaMax and 0.1% penicillin/streptomycin in Dulbecco's modified Eagle's medium/F12 media (Gibco).

Growth and culturing of immortalized human cerebromicrovascular endothelial cells (HCMEC/D3) (Sigma-Aldrich), primary HBMECs (ScienCell), human primary astrocytes (Lonza Biosciences), and human primary pericytes (ScienCell) were performed as previously reported (*27*, *97*). Briefly, HCMEC/D3 and HBMEC cells were cultured in endothelial cell media (ScienCell) supplemented with fetal bovine serum, endothelial cell growth supplement, and penicillin/streptomycin as provided by the company. Astrocyte and pericyte cells were grown in complete formulations of astrocyte cell media (ScienCell) and pericyte cell media (ScienCell), respectively. For immunostaining experiments, HCMEC/D3 and HBMEC cells were grown in type 1 rat collagen-coated plates. These endothelial cells were used below passage 20 for maintenance of their BBB properties.

Cell viability assay

Cells were plated at a density of 1500 cells per well in black-well clear-bottom 96-well plates and left growing in culture conditions overnight. Next day, cells were treated with titrating doses of the indicated compounds. For BIA-only cytotoxicity studies, cells were incubated with BIA for 96 hours. For BIA and cisplatin combinatorial studies, cells were incubated with BIA and cisplatin, and corresponding controls, for 5 days. Next, we used the Cell-Titer Glo 3D (Promega) following the provider's guidelines and quantified for luminescence signal using a Molecular Devices SpectraMax M2 plate reader. Conditions were repeated in triplicates.

Growth in low attachment assay

Fluorescently labeled GBM cells (G9-PCDH and G34-PCDH, GFP-labeled) were plated in clear ultralow attachment 96-well plates (Costar) with a density of 2000 cells per well using 100 μl of complete neurobasal medium. Then, cells were centrifuged at 1200 rpm for 3 min. Cells were treated as indicated above, and fluorescence was visualized using a Nikon Eclipse Ti2 microscope. Sphere diameter was measured using ImageJ software. Conditions were repeated in triplicates.

Synergy analysis of BIA and cisplatin combinations in GBM neurospheres in vitro

To identify whether the BIA and cisplatin combinations present synergistic antineoplastic effects in GBM cell line neurospheres, we used the SynergyFinder 3.0 software (*98*). For this, cell viability assays (see above) were performed. Concentrations of 0, 0.3, 1, and 3 μM BIA were added in combination with 0, 0.62, 1.25, 2.5, 5, and 10 μM cisplatin, accordingly, for an exposure duration of 5 days. Cell Titer Glo 3D assays were performed for cell viability assessment. SynergyFinder 3.0 analysis was done with LL4 curve fitting, with outlier correction, following a Zero Interaction Potency (ZIP) synergy score. We performed a ZIP-based analysis since this models low false-positive rates while calculating synergy of anti-oncogenic drugs (*99*). For reference, δ-scores of less than −10 could signify antagonism, −10 to 10 could signify additivity, and above 10 could signify synergism.

RNA-seq of HCMEC/D3 cells treated with BIA

For RNA-seq, HCMEC/D3 cells were plated at a density of 500,000 cells per well in a six-well plate, left to grow for 24 hours, and then treated with 1 μM BIA or dimethyl sulfoxide (DMSO; control). After 24 hours, cells were collected and processed for RNA extraction using the column-based RNeasy kit (QIAGEN), following the provider's instructions. RNA quality and quantity were quantified using a NanoDrop One (Invitrogen). At least 500 ng of RNA was submitted for bulk RNA-seq at GeneWiz (Azenta Life Sciences). Quality control (QC) was accessed, and library was prepared with poly(A) selection. Sequencing was performed using Illumina HiSeq.

Differential gene expression on the RNA-seq raw data (FASTQ files) was analyzed by Azenta Life Sciences using DESeq2 aligning to human transcriptome. Data QC was verified. Log_2FC was calculated by log_2 (BIA group mean normalized counts/control group mean normalized counts). The Wald test *P* value and Benjamini-Hochberg adjusted *P* value were calculated. A heatmap and volcano plot of top adjusted *P* value DEGs in ensemble ID annotation biclustering to treatment conditions were generated. Control and BIA groups consisted of three-independent samples.

IF staining

For IF staining of HCMEC/D3 endothelial cells, we coated eight-well Nunc Lab-Tek chamber slides (Thermo Fisher Scientific) with 1× type 1 rat tail collagen (Corning) following the provider's instructions. Then, we plated at a density of 50,000 cells per well and left in culture for 72 hours to allow for barrier formation. Next, we treated with BIA or control for 24 to 48 hours. Cells were then fixed with 10% formalin (Thermo Fisher Scientific) for 10 min, permeabilized for 30 min using 0.01% Triton X-100, and blocked with 0.1% normal donkey serum (Calbiochem) for 1 hour in 0.025% Tween 20 (Thermo Fisher Scientific) in phosphate-buffered saline (PBS) (Gibco). Then, the following primary antibodies were added: mouse anti-CDH5 (1:100; VE-cadherin, BioLegend), rabbit anti–Claudin-5 (1:100; Thermo Fisher Scientific), mouse anti–ZO-1 (1:100; Invitrogen), rabbit anti–pan-laminin (1:300; MiliporeSigma), rabbit anti-COL1A1 (1:100; Thermo Fisher Scientific), rabbit anti-ACVRL1 (1:100; Thermo Fisher Scientific), rabbit anti-ESAM (1:200; Thermo Fisher Scientific), goat anti-endoglin (1:200; R&D Systems), and mouse anti-PDGFRβ (1:100; Abcam). These primary antibodies were incubated overnight in the cold. Next day, the following secondary antibodies were used for 2 hours at room temperature: Alexa Fluor 594 anti-mouse (1:500), Alexa Fluor 594 anti-rabbit (1:500), and Alexa Fluor 647 anti-mouse (1:500), all of these were from Thermo Fisher Scientific. For cytoskeleton staining, phalloidin-iFluor 488 (1:1000; Abcam) was used for 30 min, and nuclei staining was performed using Hoechst 33342 (1:1000; Thermo Fisher Scientific) for 5 min, at room temperature.

For GBM cell staining, cells were cultured in 10% DMSO in complete neurobasal media for 2 days and then plated at a density of 50,000 cells per well in eight-well Nunc Lab-Tek chamber slides. IF staining was performed as indicated above for endothelial cells. Primary antibodies used are as follows: rabbit anti-γH2AX (Ser^{139}) (Cell Signaling Technology) at 1:100 dilution and goat anti-rabbit Alexa Fluor 647 at 1:500 dilution.

For mouse brain tissue staining, brains were collected from CO_2-euthanized and PBS-perfused tumor–bearing mice and fixed in 10% formalin for 72 hours on rotation in the cold. Then, brains were transferred to 30% sucrose for 3 days at 4°C under rotation. Before cryo-sectioning, brains were frozen at −80°C for more than 30 min, embedded in optimal cutting temperature compound (Thermo Fisher Scientific), and transferred to −21°C to a cryostat (Leica CM1950) for sectioning (20-μm thickness). Sections were placed on slides and staining followed as indicated above. All pictures were taken using a LSM 880 Zeiss confocal microscope. CDH5 quantification was performed by converting images to RGB-stack eight-bit images, and red channel fluorescence was quantified for total CDH5 and by CDH5-to-$CD31^+$ (blue channel) coverage by using the ImageJ (Fiji) software.

For GBM clinical specimen staining, tissue was fixed in 10% neutral-buffered formalin straight after collection for at least 24 hours. Then, tissue was dehydrated with an increasing ethanol gradient, cleared in xylene, and embedded in paraffin wax before microtome sectioning. Sections were done at 4-μm thickness. For IF staining, sections were deparaffinated using xylene for 5 min, twice, and rehydrated in decreasing ethanol gradients (100, 95, and 70%) for 5 min each. Slides were rinsed with distilled water to remove ethanol. Slides underwent antigen retrieval by heating in microwave for 1 to 2 min and placed in citrate buffer at pH 6 for 15 min for cooling. Blocking was done with 10% normal donkey serum for 1 hour at room temperature. Slides then were stained as mentioned above for IF imaging.

Pearson's correlation analysis for IF staining was performed using CDH5 and CD31 or GFP as costain signals. Analysis was performed using a publicly available ImageJ Colocalization Threshold Plugin, Coloc2.

BBB spheroids and dextran permeability assay

BBB spheroids were grown and cultured with a fluorescein isothiocyanate (FITC)–conjugated (70 kDa) fluorescent dextran (MilliporeSigma) as previously reported (*26*, *27*). BBB spheroids were grown for 48 hours and then treated with BIA at increasing doses for 72 hours. Then, spheroids were collected and stained as indicated above for CDH5 and F-actin (phalloidin). In the case of fluorescent dextran incubation, BBB spheroids were collected in 1.5-ml microtubes (Eppendorf) and incubated for 3 hours at 37°C. Pictures were taken by confocal microscopy. For dextran permeability measurement, we captured 21 images using Z-stack layers of 5-μm intervals for achieving a total depth of 100 μm within the sphere. Fluorescent dextran intensity from maximal intensity projection was quantified using ImageJ (National Institutes of Health).

Trans-endothelial electrical resistance

HCMEC/D3 or HBMEC cells were plated in 8W10E+ PET eight-well arrays (Applied Biophysics) at a density of 100,000 cells per well in 500 µl. These arrays were placed in a prestabilized ECIS Z-Theta instrument (Applied Biophysics). Using the ECIS Z-Theta software (Applied Biophysics), measurements were set to 4000 and 64,000 Hz every 30 min. Cells were left to grow and form a barrier for 48 to 72 hours (normally, a resistance plateau would be reached, and capacitance showed at ~10 nF for 64,000 Hz). Cells were then treated with BIA and left to grow up to 5 days, with frequent drug-containing media readdition for maintenance of the culture. Resistance (ohm) and capacitance (nF) were recorded and plotted.

Real-time PCR

Total RNA from GBM and HCMEC/D3 cells was obtained and processed as indicated above. For cDNA generation, we used 1 µg of RNA and processed with with the iScript cDNA synthesis kit (Bio-Rad), following the protocol indicated by the provider. All primers were designed using NCBI Primer-Blast tool. Detailed information on primer sequence can be found in table S3. Gene expression levels were quantified using PowerUp SYBR Green Master Mix (Applied Biosciences) on QuantStudio 6 Pro System (Applied Biosciences), normalized by housekeeping gene GAPDH expression and represented as relative expression using the comparative $\Delta\Delta C_T$ method.

Western blot

HCMEC/D3 and GBM cell lysates were collected in radioimmunoprecipitation assay buffer (Thermo Fisher Scientific) supplemented with 1× protease/phosphatase inhibitor cocktail (Cell Signaling Technology). Lysate collection from murine tumor tissue samples (~30 mg) was performed under homogenization using 23G and 26G needles. Total protein concentration was measured using the Pierce 660 nm Protein Assay Reagent (Thermo Fisher Scientific) at 660-nm absorbance in a Molecular Devices SpectraMax M2 plate reader. Samples were incubated in 1× Laemmli sample buffer (Bio-Rad) at 95°C for 5 min before loading onto 10% Mini-PROTEAN TGX precast protein gel (Bio-Rad). The PageRuler Plus Prestained Protein Ladder (Thermo Fisher Scientific) was used as a ladder. Blocking was performed in 5% milk with 0.1% Triton X-100 in 1× PBS (TBST) (Gibco) for 1 hour at room temperature under shaking. Primary antibodies used were incubated in the cold under shaking overnight: anti-pCHK1 (Ser^{345}) (1:100; Cell Signaling Technology), anti-CHK1 (1:1000; Cell Signaling Technology), anti-pH2AX (Ser^{139}) (1:1000; Cell Signaling Technology), anti-WNT7A/B (1:1000; Proteintech), anti–IL-6 (1:1000; Thermo Fisher Scientific), anti–phospho-GSK3b (Ser^{9}) (1:1000; Cell Signaling Technology), anti-vinculin (1:1000; Proteintech), anti–phospho-TYK2 (Tyr^{1054} and Tyr^{1055}) (1:1000; Thermo Fisher Scientific), anti-phospho-STAT5A/B (Tyr^{694}) (1:1000; Cell Signaling Technology), anti–phospho-p38α (Thr^{180} and Tyr^{182}) (1:1000; Thermo Fisher Scientific), anti–phospho-SRC (Tyr^{416}) (1:1000; Cell Signaling Technology), anti–phospho-CREB (Ser^{133}) (1:500; Thermo Fisher Scientific), anti-MFSD2A (1:500; Proteintech), anti-CAV1 (1:1000; Proteintech), anti-CD144 (VE-cadherin) (1:1000; Thermo Fisher Scientific), and anti–β-actin (1:2000; Cell Signaling Technology). The appropriate secondary antibody goat anti–mouse–horseradish peroxidase (HRP; Sigma-Aldrich) or goat anti–rabbit-HRP (Sigma-Aldrich) was used in 5% milk in 1× TBST with 1:5000 dilution for 1 hour at room temperature.

Phospho-kinase array

HCMEC/D3 cells were plated at a density of 1 million cells and treated with either 1 µM BIA or vehicle DMSO for 24 hours. Cell lysates were collected with the manufacturer provided lysis buffer 6 supplemented with aprotinin (10 µg/ml; Tocris), leupeptin hemisulfate (10 µg/ml; Tocris), and pepstatin A (10 µg/ml; Tocris) for protein preservation. Fifty micrograms of lysate from each sample was loaded into each membrane. All experiment procedures were performed using the Proteome Profiler Human Phospho-Kinase Array Kit (R&D Systems) following the manufacturer's protocol.

siRNA transfections

G9-PCDH and G30 cells were cultured to approximately 60% confluency and transfected using Lipofectamine RNAiMax Transfection Reagent (Invitrogen) for 1 day and then replated for Western blot or cell viability assays. All experimental steps followed the manufacturer's protocol. siCHK1 (Ambion) was used for CHK1 depletion. MISSION siRNA universal negative control (Sigma-Aldrich) was used as control siRNA.

Electroporation was performed for HCMEC/D3 cell line transfection. Briefly, 10×10^7 cells were trypsinized, washed with 1× PBS, and resuspended in resuspension R buffer (Invitrogen) at a density of 10×10^7 cells/ml. A total of 200 nM siCDH5 (Ambion, 4392420, s223070) or MISSION negative control was added to the cells. Cells with siRNA mix were transferred to a cuvette. The Neon Transfection system (Invitrogen) was set up at 1400 V and a pulse width of 20 ms for two pulses. After electroporation, cells were transferred to a well in a 24-well plate and left incubating at 37°C, 5% CO_2 for 48 hours; at this point, cells were collected for protein lysates and Western blot as indicated above.

Flow cytometry for cell cycle, DNA damage, and apoptosis assays

For cell cycle analysis, 100,000 HCMEC/D3 cells were plated in six-well plates and treated with indicated concentrations of BIA or control for 48 hours. Then, cells were washed twice with PBS and fixed/permeabilized with 5 ml of cold 70% ethanol added dropped-wise while vortexing at low speed. Cells were stored for 1 day at −20°C, washed three times with PBS, and treated with ribonuclease I (20 µg/ml; Thermo Fisher Scientific) and stained with anti-Ki-67 FITC-conjugated (1:1000) (BD Biosystems) and 1.5 µM propidium iodide (Thermo Fisher Scientific). After 30 min of incubation in the dark, cells were analyzed using a CytoFLEX system (Beckman Coulter). Fifty thousand events were counted, and data were analyzed using the CytoFLEX system software (Beckman Coulter).

For apoptosis assessment, HCMEC/D3 cells were treated as indicated above for 72 hours with BIA at indicated doses. Cells were collected from the six-well plates, washed three times with PBS, and then incubated with SYTOX Blue nucleic acid stain (5 mM) with a dilution of 1:1000 for 15 min. Cells were submitted and analyzed in the CytoFLEX system and its software as indicated above.

For DNA damage and cell cycle assessment of BIA and cisplatin, G62 cells were plated at a density of 100,000 cells per well in a six-well plate and grown in complete neurobasal media. Cells then were treated with BIA and/or cisplatin and control for 72 hours. Next, cells were collected and washed three times with PBS and stained with 1:500 of FITC anti-γH2AX phospho (Ser^{139}) (BioLegend) antibody and propidium iodide (1 mg/ml) at 1:1000 dilution for 30 min

in the dark. Cells were taken for analysis in a BD Fortessa cytometer, and data were analyzed using a FlowJo software (BD Biosciences).

Cell counts

HCMEC/D3 cells were counted and plated at a density of 300,000 cells per well in a six-well plate. After overnight growth in culture conditions, DMSO or BIA was added at 1 or 5 μM. Cells were counted every 2 days, and media with fresh BIA or DMSO was replaced for continuous growth.

Secretome quantification

For cytokine analysis of brain endothelial cells after BIA exposure, HCMEC/D3 cells were plated at a density of 500, 000 cells per well in a six-well plate. Cells were treated with indicated doses of BIA or DMSO for 48 hours. Then, 1 ml of media was collected and processed for cytokine quantification in a Luminex platform (Thermo Fisher Scientific) following the provider's instructions.

BIA and PPRX-1701 preparation

BIA powder stocks (MilliporeSigma) were resuspended in DMSO at a concentration of 10 mM (in vitro usage) or 100 mM (in vivo usage). For animal experiments, 100 mM BIA was dissolved in 2% Tween 20 (Thermo Fisher Scientific) and 1% polyethylene glycol 400 (Thermo Fisher Scientific) in sterile PBS to achieve a concentration of 10 mM BIA. PPRX-1701 was prepared and provided by Cytodigm Inc. as previously reported (*37*).

G9-TCF reporter assay

G9-TCF cells were engineered by overexpressing a luciferase gene (Luc2) controlled by a TCF7-recognized promoter in the G9-PCDH cell line. Cells were plated in 96-well dark-well clear flat bottom plates at a density of 1500 cells per well. Next day, cells were treated with increasing BIA doses for 5 hours and then exposed to D-luciferin (10 μg/ml; Goldbio). Luminescence signal was quantified in the in vivo imaging system (IVIS).

BIA quantification in vivo

G30-LRP cells were implanted in nude mice as previously indicated, left to grow for 14 days, and injected with BIA or PPRX-1701 [20 mg/kg, intraperitoneal (ip)]. After 1 hour in circulation, mice were euthanized and perfused, and tumor and brain tissue were harvested. Tissue was frozen at −80°C until processing. Quantification of BIA was performed using a Q-Exactive HFX Orbitrap mass spectrometer (liquid chromatography–high resolution mass spectrometry) (Thermo Fisher Scientific). Sample processing and analysis were performed as previously described (*37*).

In vivo studies

For intracranial tumor implantation, GBM neurospheres were grown to 70% confluency before dissociated into single cells on the day of surgery. Fifty thousand cells were resuspended in 3 μl of sterile PBS and injected intracranially into the striatum (2 mm right hemisphere, 1 mm frontal, 3 mm depth from bregma) of mice under anesthesia and stereotactically fixed. Tumors were left to grow for approximately 2 to 3 weeks, depending on the cell line. Animals were randomized to treatment groups. BIA injections consisted of 20 mg/kg (ip), except if indicated otherwise. PPRX-1701 was administered at 20 mg/kg [intravenously (iv)] via the lateral tail vein. Cisplatin injections were performed at 5 mg/kg (maximum tolerated dose, ip). All GBM tumor murine studies involved continuous condition and weight assessments, with endpoint considered when 20% of weight loss and/or moderate-to-high grimace scale and neurological symptoms were observed.

ICP-MS for platinum quantification

Mice treated with cisplatin after BIA administration were euthanized and intracardially perfused with PBS, and tissue was harvested to be stored at −80°C. Tissue was processed, and platinum (Pt195) was quantified using an Agilent 7900 ICP-MS, as previously described (*12*).

Sodium fluorescein BTB permeability studies

Sodium fluorescein was administered to G30 tumor–bearing mice intravenously via lateral tail vein at 20 mg/kg. Then, 30 min after administration when peak fluorescence is reached in the brain, mice were euthanized and and intracardially perfused for at least 1 min using 1× PBS (Gibco), for the immediate brain tissue harvest. Fresh brain samples were visualized in a Xenogen IVIS. Quantification of pixel intensities from acquired images was performed in ImageJ.

Data and statistical analysis

Numerical results were recorded, graphed, and statistically analyzed using the Prism software (GraphPad). Experiments were independently replicated at least three times, unless indicated differently in the figure legends.

Supplementary Materials

This PDF file includes:

Figs. S1 to S16
Tables S1 to S3

REFERENCES AND NOTES

1. Q. T. Ostrom, G. Cioffi, H. Gittleman, N. Patil, K. Waite, C. Kruchko, J. S. Barnholtz-Sloan, CBTRUS statistical report: Primary brain and other central nervous system tumors diagnosed in the United States in 2012-2016. *Neuro Oncol.* **21** (Suppl. 5), V1–V100 (2019).
2. S. Grochans, A. M. Cybulska, D. Simińska, J. Korbecki, K. Kojder, D. Chlubek, I. Baranowska-Bosiacka, Epidemiology of glioblastoma multiforme–literature review. *Cancers* , 2412 (2022).
3. M. D. Sweeney, Z. Zhao, A. Montagne, A. R. Nelson, B. V. Zlokovic, Blood-brain barrier: From physiology to disease and back. *Physiol. Rev.* **99**, 21–78 (2018).
4. P. S. Steeg, The blood–tumour barrier in cancer biology and therapy. *Nat. Rev. Clin. Oncol.* **18**, 696–714 (2021).
5. C. D. Arvanitis, G. B. Ferraro, R. K. Jain, The blood–brain barrier and blood–tumour barrier in brain tumours and metastases. *Nat. Rev. Cancer* **20**, 26–41 (2020).
6. P. R. Lockman, R. K. Mittapalli, K. S. Taskar, V. Rudraraju, B. Gril, K. A. Bohn, C. E. Adkins, A. Roberts, H. R. Thorsheim, J. A. Gaasch, S. Huang, D. Palmieri, P. S. Steeg, Q. R. Smith, Heterogeneous blood-tumor barrier permeability determines drug efficacy in experimental brain metastases of breast cancer. *Clin. Cancer Res.* **16**, 5664–5678 (2010).
7. C. D. Arvanitis, V. Askoxylakis, Y. Guo, M. Datta, J. Kloepper, G. B. Ferraro, M. O. Bernabeu, D. Fukumura, N. McDannold, R. K. Jain, Mechanisms of enhanced drug delivery in brain metastases with focused ultrasound-induced blood–tumor barrier disruption. *Proc. Natl. Acad. Sci. U.S.A.* **115**, E8717–E8726 (2018).
8. A. Bunevicius, N. J. McDannold, A. J. Golby, Focused ultrasound strategies for brain tumor therapy. *Oper. Neurosurg.* **19**, 9–18 (2020).
9. C. P. Sperring, M. G. Argenziano, W. M. Savage, D. E. Teasley, P. S. Upadhyayula, N. J. Winans, P. Canoll, J. N. Bruce, Convection-enhanced delivery of immunomodulatory therapy for high-grade glioma. *Neurooncol. Adv.* **5**, vdad044 (2023).
10. Q. Cai, X. Li, H. Xiong, H. Fan, X. Gao, V. Vemireddy, R. Margolis, J. Li, X. Ge, M. Giannotta, K. Hoyt, E. Maher, R. Bachoo, Z. Qin, Optical blood-brain-tumor barrier modulation expands therapeutic options for glioblastoma treatment. *Nat. Commun.* **14**, 4934 (2023).
11. J. V. Gregory, P. Kadiyala, R. Doherty, M. Cadena, S. Habeel, E. Ruoslahti, P. R. Lowenstein, M. G. Castro, J. Lahann, Systemic brain tumor delivery of synthetic protein nanoparticles for glioblastoma therapy. *Nat. Commun.* **11**, 5687 (2020).

12. J. L. Jimenez-Macias, Y. C. Lee, E. Miller, T. Finkelberg, M. Zdioruk, G. Berger, C. E. Farquhar, M. O. Nowicki, C. F. Cho, B. I. Fedeles, A. Loas, B. L. Pentelute, S. E. Lawler, A Pt(IV)-conjugated brain penetrant macrocyclic peptide shows pre-clinical efficacy in glioblastoma. *J. Control. Release* **352**, 623–636 (2022).
13. S. P. Williams, M. O. Nowicki, F. Liu, R. Press, J. Godlewski, M. Abdel-Rasoul, B. Kaur, S. A. Fernandez, E. A. Chiocca, S. E. Lawler, Indirubins decrease glioma invasion by blocking migratory phenotypes in both the tumor and stromal endothelial cell compartments. *Cancer Res.* **71**, 5374–5380 (2011).
14. L. Yang, X. Li, W. Huang, X. Rao, Y. Lai, Pharmacological properties of indirubin and its derivatives. *Biomed. Pharmacother.* **151**, 113112 (2022).
15. L. Meijer, A.-L. Skaltsounis, P. Magiatis, P. Polychronopoulos, M. Knockaert, M. Leost, X. P. Ryan, C. Alin Vonica, A. Brivanlou, R. Dajani, A. Musacchio, S. M. Roe, L. Pearl, P. Greengard, GSK-3-selective inhibitors derived from tyrian purple indirubins. *Chem. Biol.* **10**, 1255–1266 (2003).
16. I. A. Schepetkin, M. B. Plotnikov, A. I. Khlebnikov, T. M. Plotnikova, M. T. Quinn, Oximes: Novel therapeutics with anticancer and anti-inflammatory potential. *Biomolecules* **11**, 777 (2021).
17. P. Dusart, B. M. Hallström, T. Renné, J. Odeberg, M. Uhlén, L. M. Butler, A systems-based map of human brain cell-type enriched genes and malignancy-associated endothelial changes. *Cell Rep.* **29**, 1690–1706.e4 (2019).
18. T. Wälchli, M. Ghobrial, M. Schwab, S. Takada, H. Zhong, S. Suntharalingham, S. Vetiska, D. R. Gonzalez, R. Wu, H. Rehrauer, A. Dinesh, K. Yu, E. L. Y. Chen, J. Bisschop, F. Farnhammer, A. Mansur, J. Kalucka, I. Tirosh, L. Regli, K. Schaller, K. Frei, T. Ketela, M. Bernstein, P. Kongkham, P. Carmeliet, T. Valiante, P. B. Dirks, M. L. Suva, G. Zadeh, V. Tabar, R. Schlapbach, H. W. Jackson, K. De Bock, J. E. Fish, P. P. Monnier, G. D. Bader, I. Radovanovic, Single-cell atlas of the human brain vasculature across development, adulthood and disease. *Nature* **632**, 603–613 (2024).
19. W. Li, Z. Chen, I. Chin, Z. Chen, H. Dai, The role of VE-cadherin in blood-brain barrier integrity under central nervous system pathological conditions. *Curr. Neuropharmacol.* **16**, 1375–1384 (2018).
20. V. M. Ravi, P. Will, J. Kueckelhaus, N. Sun, K. Joseph, H. Salié, L. Vollmer, U. Kuliesiute, J. von Ehr, J. K. Benotmane, N. Neidert, M. Follo, F. Scherer, J. M. Goeldner, S. P. Behringer, P. Franco, M. Khiat, J. Zhang, U. G. Hofmann, C. Fung, F. L. Ricklefs, K. Lamszus, M. Boerries, M. Ku, J. Beck, R. Sankowski, M. Schwabenland, M. Prinz, U. Schüller, S. Killmer, B. Bengsch, A. K. Walch, D. Delev, O. Schnell, D. H. Heiland, Spatially resolved multi-omics deciphers bidirectional tumor-host interdependence in glioblastoma. *Cancer Cell* **40**, 639–655.e13 (2022).
21. T. N. Phoenix, D. M. Patmore, S. Boop, N. Boulos, M. O. Jacus, Y. T. Patel, M. F. Roussel, D. Finkelstein, L. Goumnerova, S. Perreault, E. Wadhwa, Y. J. Cho, C. F. Stewart, R. J. Gilbertson, medulloblastoma genotype dictates blood brain barrier phenotype. *Cancer Cell* **29**, 508–522 (2016).
22. A. Griveau, G. Seano, S. J. Shelton, R. Kupp, A. Jahangiri, K. Obernier, S. Krishnan, O. R. Lindberg, T. J. Yuen, A. C. Tien, J. K. Sabo, N. Wang, I. Chen, J. Kloepper, L. Larrouquere, M. Ghosh, I. Tirosh, E. Huillard, A. Alvarez-Buylla, M. C. Oldham, A. I. Persson, W. A. Weiss, T. T. Batchelor, A. Stemmer-Rachamimov, M. L. Suvà, J. J. Phillips, M. K. Aghi, S. Mehta, R. K. Jain, D. H. Rowitch, A glial signature and Wnt7 signaling regulate glioma-vascular interactions and tumor microenvironment. *Cancer Cell* **33**, 874–889.e7 (2018).
23. O. K. Provance, V. O. Oria, T. T. Tran, J. I. Caulfield, C. R. Zito, A. Aguirre-Ducler, K. A. Schalper, H. M. Kluger, L. B. Jilaveanu, Vascular mimicry as a facilitator of melanoma brain metastasis. *Cell. Mol. Life Sci.* **81**, 188 (2024).
24. K. Maddison, N. A. Bowden, M. C. Graves, P. A. Tooney, Characteristics of vasculogenic mimicry and tumour to endothelial transdifferentiation in human glioblastoma: A systematic review. *BMC Cancer* **23**, 185 (2023).
25. X. G. Mao, X. Y. Xue, L. Wang, X. Zhang, M. Yan, Y. Y. Tu, W. Lin, X. F. Jiang, H. G. Ren, W. Zhang, S. J. Song, CDH5 is specifically activated in glioblastoma stemlike cells and contributes to vasculogenic mimicry induced by hypoxia. *Neuro Oncol.* **15**, 865–879 (2013).
26. C. F. Cho, J. M. Wolfe, C. M. Fadzen, D. Calligaris, K. Hornburg, E. A. Chiocca, N. Y. R. Agar, B. L. Pentelute, S. E. Lawler, Blood-brain-barrier spheroids as an in vitro screening platform for brain-penetrating agents. *Nat. Commun.* **8**, 1–14 (2017).
27. S. Bergmann, S. E. Lawler, Y. Qu, C. M. Fadzen, J. M. Wolfe, M. S. Regan, B. L. Pentelute, N. Y. R. Agar, C. F. Cho, Blood–brain-barrier organoids for investigating the permeability of CNS therapeutics. *Nat. Protoc.* **13**, 2827–2843 (2018).
28. J. M. Wolfe, C. M. Fadzen, R. L. Holden, M. Yao, G. J. Hanson, B. L. Pentelute, Perfluoroaryl bicyclic cell-penetrating peptides for delivery of antisense oligonucleotides. *Angew. Chem. Int. Ed. Engl.* **57**, 4756–4759 (2018).
29. R. Hoessel, S. Leclerc, J. A. Endicott, M. E. M. Nobel, A. Lawrie, P. Tunnah, M. Leost, E. Damiens, D. Marie, D. Marko, E. Niederberger, W. Tang, G. Eisenbrand, L. Meijer, Indirubin, the active constituent of a Chinese antileukaemia medicine, inhibits cyclin-dependent kinases. *Nat. Cell Biol.* **1**, 60–67 (1999).
30. H. Kanki, T. Sasaki, S. Matsumura, T. Kawano, K. Todo, S. Okazaki, K. Nishiyama, H. Takemori, H. Mochizuki, CREB coactivator CRTC2 plays a crucial role in endothelial function. *J. Neurosci.* **40**, 9533–9546 (2020).
31. L. D. Mayo, K. M. Kessler, R. Pincheira, R. S. Warren, D. B. Donner, Vascular endothelial cell growth factor activates CRE-binding protein by signaling through the KDR receptor tyrosine kinase. *J. Biol. Chem.* **276**, 25184–25189 (2001).
32. J. A. Gustin, R. Pincheira, L. D. Mayo, O. N. Ozes, K. M. Kessler, M. R. Baerwald, C. K. Korgaonkar, D. B. Donner, C.-D. K. Korgaonkar, Tumor necrosis factor activates CRE-binding protein through a p38 MAPK/MSK1 signaling pathway in endothelial cells. *Am. J. Physiol. Cell Physiol.* **286**, C547–C555 (2004).
33. X. Xi, N. Liu, Q. Wang, Y. Chu, Z. Yin, Y. Ding, Y. Lu, ACT001, a novel PAI-1 inhibitor, exerts synergistic effects in combination with cisplatin by inhibiting PI3K/AKT pathway in glioma. *Cell Death Dis.* **10**, 757 (2019).
34. M. Wu, Y. Wang, D. Yang, Y. Gong, F. Rao, R. Liu, Y. Danna, J. Li, J. Fan, J. Chen, W. Zhang, Q. Zhan, A PLK1 kinase inhibitor enhances the chemosensitivity of cisplatin by inducing pyroptosis in oesophageal squamous cell carcinoma. *EBioMedicine* **41**, 244–255 (2019).
35. A. Lopergolo, V. Nicolini, E. Favini, L. D. Bo, M. Tortoreto, D. Cominetti, M. Folini, P. Perego, V. Castiglioni, E. Scanziani, M. G. Borrello, N. Zaffaroni, G. Cassinelli, C. Lanzi, Synergistic cooperation between sunitinib and cisplatin promotes apoptotic cell death in human medullary thyroid cancer. *J. Clin. Endocrinol. Metabol.* **99**, 498–509 (2014).
36. Z. Qiu, N. L. Oleinick, J. Zhang, ATR/CHK1 inhibitors and cancer therapy. *Radiother. Oncol.* **126**, 450–464 (2018).
37. M. Zdioruk, J. L. Jimenez-Macias, M. O. Nowicki, K. E. Manz, K. D. Pennell, M. S. Koch, T. Finkelberg, B. Wu, P. Boucher, Y. Takeda, W. Li, R. Piranlioglu, A. L. Ling, E. A. Chiocca, S. E. Lawler, PPRX-1701, a nanoparticle formulation of 6′-bromoindirubin acetoxime, improves delivery and shows efficacy in preclinical GBM models. *Cell Rep. Med.* **4**, 101019 (2023).
38. M. Asheuer, F. Pflumio, S. Benhamida, A. Dubart-Kupperschmitt, F. Fouquet, Y. Imai, P. Aubourg, N. Cartier, Human $CD34^+$ cells differentiate into microglia and express recombinant therapeutic protein. *Proc. Natl. Acad. Sci. U.S.A.* **101**, 3557–3562 (2004).
39. N. Davoust, C. Vuaillat, G. Cavillon, C. Domenget, E. Hatterer, A. Bernard, C. Dumontel, P. Jurdic, C. Malcus, C. Confavreux, M. F. Belin, S. Nataf, Bone marrow CD34+/B220+ progenitors target the inflamed brain and display in vitro differentiation potential toward microglia. *FASEB J.* **20**, 2081–2092 (2006).
40. M. A. Haber, A. Iranmahboob, C. Thomas, M. Liu, A. Najjar, D. Zagzag, ERG is a novel and reliable marker for endothelial cells in central nervous system tumors. *Clin. Neuropathol.* **34**, 117–127 (2015).
41. L. Fina, H. V. Molgaard, D. Robertson, N. J. Bradley, P. Monaghan, D. Delia, D. R. Sutherland, M. A. Baker, M. F. Greaves, Expression of the CD34 Gene in Vascular Endothelial Cells. *Blood* **75**, 2417–2426 (1990).
42. M. Hassanpour, A. A. Salybekov, S. Kobayashi, T. Asahara, CD34 positive cells as endothelial progenitor cells in biology and medicine. *Front. Cell Dev. Biol.* **11**, 1128134 (2023).
43. M. J. Siemerink, I. Klaassen, I. M. C. Vogels, A. W. Griffioen, C. J. F. Van Noorden, R. O. Schlingemann, CD34 marks angiogenic tip cells in human vascular endothelial cell cultures. *Angiogenesis* **15**, 151–163 (2012).
44. E. J. Yee, I. Vigil, Y. Sun, R. J. Torphy, R. D. Schulick, Y. Zhu, Group XIV C-type lectins: Emerging targets in tumor angiogenesis. *Angiogenesis* **27**, 173–192 (2024).
45. J. Robinson, K. Whitworth, E. Jinks, Z. Nagy, R. Bicknell, S. P. Lee, An evaluation of the tumour endothelial marker CLEC14A as a therapeutic target in solid tumours. *J. Pathol. Clin. Res.* **6**, 308–319 (2020).
46. X. Zhuang, F. Maione, J. Robinson, M. Bentley, B. Kaul, K. Whitworth, N. Jumbu, E. Jinks, J. Bystrom, P. Gabriele, E. Garibaldi, E. Delmastro, Z. Nagy, D. Gilham, E. Giraudo, R. Bicknell, S. P. Lee, CAR T cells targeting tumor endothelial marker CLEC14A inhibit tumor growth. *JCI Insight* **5**, e138808 (2020).
47. M. Bocci, J. Sjölund, E. Kurzejamska, D. Lindgren, N. A. D. Marzouka, M. Bartoschek, M. Höglund, K. Pietras, Activin receptor-like kinase 1 is associated with immune cell infiltration and regulates CLEC14A transcription in cancer. *Angiogenesis* **22**, 117–131 (2019).
48. Y. Xie, L. He, R. Lugano, Y. Zhang, H. Cao, Q. He, M. Chao, B. Liu, Q. Cao, J. Wang, Y. Jiao, Y. Hu, L. Han, Y. Zhang, H. Huang, L. Uhrbom, C. Betsholtz, L. Wang, A. Dimberg, L. Zhang, Key molecular alterations in endothelial cells in human glioblastoma uncovered through single-cell RNA sequencing. *JCI Insight* **6**, e150861 (2021).
49. J. Schaffenrath, T. Wyss, L. He, E. J. Rushing, M. Delorenzi, F. Vasella, L. Regli, M. C. Neidert, A. Keller, Blood-brain barrier alterations in human brain tumors revealed by genome-wide transcriptomic profiling. *Neuro Oncol.* **23**, 2095–2106 (2021).
50. Z. Cui, H. Wu, Y. Xiao, T. Xu, J. Jia, H. Lin, R. Lin, K. Chen, Y. Lin, K. Li, X. Wu, C. Li, B. Yu, Endothelial PDGF-BB/PDGFR-β signaling promotes osteoarthritis by enhancing angiogenesis-dependent abnormal subchondral bone formation. *Bone Res.* **10**, 58 (2022).
51. W. Chen, Y. Guo, E. J. Walker, F. Shen, K. Jun, S. P. Oh, V. Degos, M. T. Lawton, T. Tihan, D. Davalos, K. Akassoglou, J. Nelson, J. Pile-Spellman, H. Su, W. L. Young, Reduced mural

cell coverage and impaired vessel integrity after angiogenic stimulation in the Alk1-deficient brain. *Arterioscler. Thromb. Vasc. Biol.* **33**, 305–310 (2013).
52. L. Ruiz-Llorente, E. Gallardo-Vara, E. Rossi, D. M. Smadja, L. M. Botella, C. Bernabeu, Endoglin and alk1 as therapeutic targets for hereditary hemorrhagic telangiectasia. *Expert Opin. Ther. Targets* **21**, 933–947 (2017).
53. H. Cai, W. Liu, Y. Xue, X. Shang, J. Liu, Z. Li, P. Wang, L. Liu, Y. Hu, Y. Liu, Roundabout 4 regulates blood-tumor barrier permeability through the modulation of ZO-1, occludin, and claudin-5 expression. *J. Neuropathol. Exp. Neurol.* **74**, 25–27 (2014).
54. C. A. Jones, N. R. London, H. Chen, K. W. Park, D. Sauvaget, R. A. Stockton, J. D. Wythe, W. Suh, F. Larrieu-Lahargue, Y. S. Mukouyama, P. Lindblom, P. Seth, A. Frias, N. Nishiya, M. H. Ginsberg, H. Gerhardt, K. Zhang, D. Y. Li, Robo4 stabilizes the vascular network by inhibiting pathologic angiogenesis and endothelial hyperpermeability. *Nat. Med.* **14**, 448–453 (2008).
55. W. Zheng, A. Q. Geng, P. F. Li, Y. Wang, X. B. Yuan, Robo4 regulates the radial migration of newborn neurons in developing neocortex. *Cereb. Cortex* **22**, 2587–2601 (2012).
56. J. Rakotomamonjy, L. Rylaarsdam, L. Fares-Taie, S. McDermott, D. Davies, G. Yang, F. Fagbemi, M. Epstein, M. Fairbanks-Santana, J. M. Rozet, A. Guemez-Gamboa, PCDH12 loss results in premature neuronal differentiation and impeded migration in a cortical organoid model. *Cell Rep.* **42**, 112845 (2023).
57. C. Rampon, M. H. Prandini, S. Bouillot, H. Pointu, E. Tillet, R. Frank, M. Vernet, P. Huber, Protocadherin 12 (VE-cadherin 2) is expressed in endothelial, trophoblast, and mesangial cells. *Exp. Cell Res.* **302**, 48–60 (2005).
58. S. Das, P. A. Marsden, Angiogenesis in Glioblastoma. *N. Engl. J. Med.* **369**, 1561–1563 (2013).
59. Y. Li, Q. Wu, J. Lv, J. Gu, A comprehensive pan-cancer analysis of CDH5 in immunological response. *Front. Immunol.* **14**, 1239875 (2023).
60. J. H. Seo, T. Maki, M. Maeda, N. Miyamoto, A. C. Liang, K. Hayakawa, L. D. D. Pham, F. Suwa, A. Taguchi, T. Matsuyama, M. Ihara, K. W. Kim, E. H. Lo, K. Arai, Oligodendrocyte precursor cells support blood-brain barrier integrity via TGF-β signaling. *PLOS ONE* **9**, e103174 (2014).
61. L. Schumacher, R. Slimani, L. Zizmare, J. Ehlers, F. Kleine Borgmann, J. C. Fitzgerald, P. Fallier-Becker, A. Beckmann, A. Grißmer, C. Meier, A. El-Ayoubi, K. Devraj, M. Mittelbronn, C. Trautwein, U. Naumann, TGF-beta modulates the integrity of the blood brain barrier in vitro, and is associated with metabolic alterations in pericytes. *Biomedicine* **11**, 214 (2023).
62. Y. Wang, C. Cho, J. Williams, P. M. Smallwood, C. Zhang, H. J. Junge, J. Nathans, Interplay of the Norrin and Wnt7a/Wnt7b signaling systems in blood–brain barrier and blood–retina barrier development and maintenance. *Proc. Natl. Acad. Sci. U.S.A.* **115**, E11827–E11836 (2018).
63. J. Chang, M. R. Mancuso, C. Maier, X. Liang, K. Yuki, L. Yang, J. W. Kwong, J. Wang, V. Rao, M. Vallon, C. Kosinski, J. J. H. Zhang, A. T. Mah, L. Xu, L. Li, S. Gholamin, T. F. Reyes, R. Li, F. Kuhnert, X. Han, J. Yuan, S. H. Chiou, A. D. Brettman, L. Daly, D. C. Corney, S. H. Cheshier, L. D. Shortliffe, X. Wu, M. Snyder, P. Chan, R. G. Giffard, H. Y. Chang, K. Andreasson, C. J. Kuo, Gpr124 is essential for blood-brain barrier integrity in central nervous system disease. *Nat. Med.* **23**, 450–460 (2017).
64. F. Sivandzade, L. Cucullo, In-vitro blood-brain barrier modeling: A review of modern and fast-advancing technologies. *J. Cereb. Blood Flow Metab.* **38**, 1667–1681 (2018).
65. H. C. Helms, N. J. Abbott, M. Burek, R. Cecchelli, P.-O. Couraud, M. A. Deli, C. Förster, H. J. Galla, I. A. Romero, E. V. Shusta, M. J. Stebbins, E. Vandenhaute, B. Weksler, B. Brodin, In vitro models of the blood-brain barrier: An overview of commonly used brain endothelial cell culture models and guidelines for their use. *J. Cereb. Blood Flow Metab.* **36**, 862–890 (2016).
66. V. Rani, A. Prabhu, In vitro blood brain barrier models: Molecular aspects and therapeutic strategies in glioma management. *Curr. Res. Transl. Med.* **71**, 103376 (2023).
67. T. B. Terrell-Hall, A. G. Ammer, J. I. G. Griffith, P. R. Lockman, Permeability across a novel microfluidic blood-tumor barrier model. *Fluids Barriers CNS* **14**, 3 (2017).
68. T. D. Brown, M. Nowak, A. V. Bayles, B. Prabhakarpandian, P. Karande, J. Lahann, M. E. Helgeson, S. Mitragotri, A microfluidic model of human brain (μHuB) for assessment of blood brain barrier. *Bioeng. Transl. Med.* **4**, e10126 (2019).
69. G. Adriani, D. Ma, A. Pavesi, E. L. K. Goh, R. D. Kamm, "Modeling the blood-brain barrier in a 3D triple co-culture microfluidic system" in *2015 37th Annual International Conference of the IEEE Engineering in Medicine and Biology Society (EMBC)* (IEEE, 2015), pp. 338–341.
70. H. Sherman, A. E. Rossi, A novel three-dimensional glioma blood-brain barrier model for high-throughput testing of tumoricidal capability. *Front. Oncol.* **9**, 10.3389/fonc.2019.00351 (2019).
71. S. S. Basu, N. Y. R. Agar, Bringing matrix-assisted laser desorption/ionization mass spectrometry imaging to the clinics. *Clin. Lab. Med.* **41**, 309–324 (2021).
72. S. Theiner, C. Kornauth, H. P. Varbanov, M. Galanski, S. Van Schoonhoven, P. Heffeter, W. Berger, A. E. Egger, B. K. Keppler, Tumor microenvironment in focus: LA-ICP-MS bioimaging of a preclinical tumor model upon treatment with platinum(IV)-based anticancer agents. *Metallomics* **7**, 1256–1264 (2015).
73. X. Cui, G. Pan, Y. Chen, X. Guo, T. Liu, J. Zhang, X. Yang, M. Cheng, H. Gao, F. Jiang, The p53 pathway in vasculature revisited: A therapeutic target for pathological vascular remodeling? *Pharmacol. Res.* **169**, 105683 (2021).
74. M. L. Bochenek, T. Bauer, R. Gogiraju, Y. Nadir, A. Mann, T. Schönfelder, L. Hünig, B. Brenner, T. Münzel, P. Wenzel, S. Konstantinides, K. Schäfer, The endothelial tumor suppressor p53 is essential for venous thrombus formation in aged mice. *Blood Adv.* **2**, 1300–1314 (2018).
75. G. H. H. Chan, E. Chan, C. T. K. Kwok, G. P. H. Leung, S. M. Y. Lee, S. W. Seto, The role of p53 in the alternation of vascular functions. *Front. Pharmacol.* **13**, 981152 (2022).
76. V. Kalna, Y. Yang, C. R. Peghaire, K. Frudd, R. Hannah, A. V. Shah, L. Osuna Almagro, J. J. Boyle, B. Göttgens, J. Ferrer, A. M. Randi, G. M. Birdsey, The transcription factor ERG regulates super-enhancers associated with an endothelial-specific gene expression Program. *Circ. Res.* **124**, 1337–1349 (2019).
77. Y. Zhao, J. Cao, A. Melamed, M. Worley, A. Gockley, D. Jones, H. T. Nia, Y. Zhang, T. Stylianopoulos, A. S. Kumar, F. Mpekris, M. Datta, Y. Sun, L. Wu, X. Gao, O. Yeku, M. G. Del Carmen, D. R. Spriggs, R. K. Jain, L. Xu, Losartan treatment enhances chemotherapy efficacy and reduces ascites in ovarian cancer models by normalizing the tumor stroma. *Proc. Natl. Acad. Sci. U.S.A.* **116**, 2210–2219 (2019).
78. V. P. Chauhan, J. D. Martin, H. Liu, D. A. Lacorre, S. R. Jain, S. V. Kozin, T. Stylianopoulos, A. S. Mousa, X. Han, P. Adstamongkonkul, Z. Popović, P. Huang, M. G. Bawendi, Y. Boucher, R. K. Jain, Angiotensin inhibition enhances drug delivery and potentiates chemotherapy by decompressing tumour blood vessels. *Nat. Commun.* **4**, 2516 (2013).
79. S. Wan, X. Chen, F. Yin, S. Li, Y. Zhang, H. Luo, Z. Luo, N. Cui, Y. Chen, X. Li, L. Kong, X. Wang, Indirubin derivatives as bifunctional molecules inducing DNA damage and targeting PARP for the treatment of cancer. *Eur. J. Med. Chem.* **261**, 115843 (2023).
80. M. Naganuma, S. Sugimoto, T. Fukuda, K. Mitsuyama, T. Kobayashi, N. Yoshimura, H. Ohi, S. Tanaka, A. Andoh, N. Ohmiya, K. Saigusa, T. Yamamoto, Y. Morohoshi, H. Ichikawa, K. Matsuoka, T. Hisamatsu, K. Watanabe, S. Mizuno, T. Abe, Y. Suzuki, T. Kanai, M. Naganuma, Y. Nakazato, T. Teratani, H. Ogata, Y. Iwao, H. Yamasaki, T. Toyonaga, M. Nakano, T. Hibi, Y. Sameshima, R. Hayashi, Y. Ueno, S. Bamba, M. Watanabe, A. Nakazawa, Y. Koike, J. Imai, T. Shimoyama, K. Takeuchi, M. Nagasaka, A. Kitano, S. Ashizuka, H. Inatsu, K. Onodera, H. Nakase, K. Kitamura, K. Ikeya, H. Hanai, C. Watanabe, R. Hokari, F. Hirai, Y. Naito, N. Hoshi, F. Kinjo, Y. Ishiguro, M. Sasaki, T. Matsumoto, F. Sano, R. Roberts, W. Suda, M. Hattori, S. Fukuda, A. Hirayama, Indigo naturalis is effective even in treatment-refractory patients with ulcerative colitis: A post hoc analysis from the INDIGO study. *J. Gastroenterol.* **55**, 169–180 (2020).
81. Y. Matsuno, A. Hirano, T. Torisu, Y. Okamoto, Y. Fuyuno, S. Fujioka, J. Umeno, T. Moriyama, S. Nagai, Y. Hori, M. Fujiwara, T. Kitazono, M. Esaki, Short-term and long-term outcomes of indigo naturalis treatment for inflammatory bowel disease. *J. Gastroenterol. Hepatol.* **35**, 412–417 (2020).
82. F. Chen, L. Li, D. Ma, S. Yan, J. Sun, M. Zhang, C. Ji, M. Hou, Imatinib achieved complete cytogenetic response in a CML patient received 32-year indirubin and its derivative treatment. *Leukemia Res.* **34**, e75–e77 (2010).
83. A. Nair, S. Jacob, A simple practice guide for dose conversion between animals and human. *J Basic Clin Pharm* **7**, 27–31 (2016).
84. R. K. Jain, Normalizing tumor microenvironment to treat cancer: Bench to bedside to biomarkers. *J. Clin. Oncol.* **31**, 2205–2218 (2013).
85. R. K. Jain, Barriers to drug delivery in solid tumors. *Tissue Barriers* **271**, 58–65 (1994).
86. P. Carmeliet, R. K. Jain, Principles and mechanisms of vessel normalization for cancer and other angiogenic diseases. *Nat. Rev. Drug Discov.* **10**, 417–427 (2011).
87. X. Dong, J. Ren, Z. Amoozgar, S. Lee, M. Datta, S. Roberge, M. Duquette, D. Fukumura, R. K. Jain, Anti-VEGF therapy improves EGFR-vIII-CAR-T cell delivery and efficacy in syngeneic glioblastoma models in mice. *J. Immunother. Cancer* **11**, e005583 (2023).
88. K. H. Narsinh, E. Perez, A. F. Haddad, J. S. Young, L. Savastano, J. E. Villanueva-Meyer, E. Winkler, J. de Groot, Strategies to improve drug delivery across the blood–brain barrier for glioblastoma. *Curr. Neurol. Neurosci. Rep.* **24**, 123–129 (2024).
89. Y. Gusev, K. Bhuvaneshwar, L. Song, J. C. Zenklusen, H. Fine, S. Madhavan, The REMBRANDT study, a large collection of genomic data from brain cancer patients. *Sci. Data* **5**, 180158 (2018).
90. Z. Xie, A. Bailey, M. Kuleshov, D. Clarke, J. Evangelista, S. Jenkins, A. Lachmann, M. Wojciechowicz, E. Kropiwnicki, K. Jagodnik, M. Jeon, A. Ma'ayan, Gene set knowledge discovery with Enrichr. *Curr. Protoc.* **1**, (2021).
91. M. Kuleshov, M. Jones, A. Rouillard, N. Fernandez, Q. Duan, Z. Wang, S. Koplev, S. Jenkins, K. Jagodnik, A. Lachmann, M. McDermott, C. Monteiro, G. Gundersen, A. Ma'ayan, Enrichr: A comprehensive gene set enrichment analysis web server 2016 update. *Nucleic Acids Res.* **44**, W90–W97 (2016).
92. E. Chen, C. Tan, Y. Kou, Q. Duan, Z. Wang, G. Meirelles, N. Clark, Enrichr: Interactive and collaborative HTML5 gene list enrichment analysis tool. *BMC Bioinformatics* **128**, 128 (2013).
93. D. J. B. Clarke, M. Jeon, D. J. Stein, N. Moiseyev, E. Kropiwnicki, C. Dai, Z. Xie, M. L. Wojciechowicz, S. Litz, J. Hom, J. E. Evangelista, L. Goldman, S. Zhang, C. Yoon, T. Ahamed, S. Bhuiyan, M. Cheng, J. Karam, K. M. Jagodnik, I. Shu, A. Lachmann, S. Ayling,

S. L. Jenkins, A. Ma'ayan, Appyters: Turning jupyter notebooks into data-driven web apps. *Patterns* **2**, 100213 (2021).
94. D. Szklarczyk, R. Kirsch, M. Koutrouli, K. Nastou, F. Mehryary, R. Hachilif, T. Fang, N. Doncheva, S. Pyysalo, P. Bork, L. Jensen, C. von Mering, The STRING database in 2023: Protein–protein association networks and functional enrichment analyses for any sequenced genome of interest. *Nucleic Acid Res.* **6**, D638–D646 (2023).
95. J. Kueckelhaus, S. Frerich, J. Kada-Benotmane, C. Koupourtidou, J. Ninkovic, M. Dichgans, J. Beck, O. Schnell, F. S. Heiland D, Inferring histology-associated gene expression gradients in spatial transcriptomic studies. *Nat Comm* **15**, 7280 (2024).
96. C. M. Fadzen, J. M. Wolfe, W. Zhou, C. F. Cho, N. Von Spreckelsen, K. T. Hutchinson, Y. C. Lee, E. A. Chiocca, S. E. Lawler, O. H. Yilmaz, S. J. Lippard, B. L. Pentelute, A platinum(IV) prodrug - perfluoroaryl macrocyclic peptide conjugate enhances platinum uptake in the brain. *J. Med. Chem.* **63**, 6741–6747 (2020).
97. C. M. Fadzen, J. M. Wolfe, C.-F. Cho, E. A. Chiocca, S. E. Lawler, B. L. Pentelute, Perfluoroarene–based peptide macrocycles to enhance penetration across the blood–brain barrier. *J. Am. Chem. Soc.* **139**, 15628–15631 (2017).
98. A. Ianevski, A. K. Giri, T. Aittokallio, SynergyFinder 3.0: An interactive analysis and consensus interpretation of multi-drug synergies across multiple samples. *Nucleic Acids Res.* **50**, W739–W743 (2022).
99. B. Yadav, K. Wennerberg, T. Aittokallio, J. Tang, Searching for drug synergy in complex dose-response landscapes using an interaction potency model. *Comput. Struct. Biotechnol. J.* **13**, 504–513 (2015).

Acknowledgments: This work is dedicated to the memory of our coauthor, colleague, and friend, A.B., who passed away after submission of the paper. **Funding:** This work was supported by NCI R01CA237063 (S.E.L.) and NCI R21CA259734 (S.E.L. 2023-2025 $250,000) grants. C.-F.C. is supported by the R01 CA272573-01. Support for the ICP-MS instrumentation and analysis was provided by a core center grant P30-ES002109 from the National Institute of Environmental Health Sciences, National Institutes of Health. B.I.F. was supported by National Institutes of Health grants R01-CA080024 and P30-ES002109. The Thermo LC Orbitrap MS was supported by a National Science Foundation MRI award (1919870, K.D.P.) and the NIEHS Training in Environmental Pathology T32 program T32ES007272 (K.E.M.). **Author contributions:** J.L.J.-M., A.B., B.W., A.B., and S.E.L. contributed to the writing—original draft; J.L.J.-M.,M.F., B.W., A.B., N.M., A.S.B., and S.E.L. contributed to conceptualization; J.L.J.-M., P.V.-B., A.B., M.F., A.S., K.E.M., W.H., J.C., T.L., N.M., Z.X., K.H., K.D.P., J.H., M.S., A.S.B., and S.E.L. contributed to investigation; J.L.J.-M., A.B., C.-F.C., K.D.P., N.M., A.S.B., and S.E.L. participated in writing—review and editing; J.L.J.-M., A.B., C.-F.C., M.O.N., K.E.M., N.M., M.Z., P.B., A.B., and S.E.L. offered methodology; A.B., J.R., B.W., M.O.N., W.H., J.C., K.H., B.I.F., W.L., P.B., M.P., A.B., and S.E.L. provided resources; A.B., A.B., B.W., and S.E.L. acquired funding; A.B., B.W., A.B., and S.E.L. performed data curation; J.L.J.-M., P.V.-B., A.B., A.S., K.E.M., N.M., Z.X., and S.E.L. performed validation; J.L.J.-M., P.V.-B., A.B., B.W., A.B., and S.E.L. supervised the execution of this work; J.L.J.-M., P.V.-B., M.F., A.B., J.C., Z.X., A.B., and S.E.L. performed formal analysis of results; A.B. and A.S.B. used software; J.L.J.-M., P.V.-B., A.B., B.W., T.L., A.B., and S.E.L. did the project administration; J.L.J.-M., A.B., M.F., N.M., Z.X., A.B., and S.E.L. generated visualization. **Competing interests:** B.W. has ownership interests in both Cytodigm Inc. and Phosphorex LLC. B.W. is also a board member, officer, and employee of Phosphorex,LLC. In addition, B.W. has patents US10,039,829, US10,675,350, WO2013/192493, and WO2018/025075. S.E.L. and J.L.J.-M. has US Provisional Patent Application No. 63/495,992 (13 April 2023). W.L. was an employee of Phosphorex Inc. and a current employee of Prime Medicine. T.L. was an employee of Phosphorex Inc. and a current employee of Phosphorex LLC. The authors declare that they have no other competing interests. **Data and materials availability:** Datasets used for identification of the GBM endothelium–enriched transcripts are available at cBio and GlioVis portals. Spatial transcriptomic reanalysis and single-cell RNA-seq from endothelial cells visualization are available from published datasets in (*18*, *20*), respectively. Differential gene expression analysis of RNA-seq data of BIA treatment in brain endothelial HCMEC/D3 cells can be accessed on Figshare: 10.6084/m9.figshare.28087544. All data needed to evaluate the conclusions in the paper are present in the paper and/or the Supplementary Materials. PPRX-1701 can be provided by Cytodigm Inc. pending scientific review and a completed material transfer agreement. Requests for PPRX-1701 should be should be submitted to B.W. at bwu@cytodigm.com, Cytodigm Inc.

Submitted 17 June 2024
Accepted 24 January 2025
Published 26 February 2025
10.1126/sciadv.adr1481